BUBL-1 is essential for intermediate filament organization and apical membrane morphology

Sanne Remmelzwaal[1], Florian Geisler[2], Riccardo Stucchi[3,4,5], Suzanne van der Horst[6,7], Milena Pasolli[3], Jason R. Kroll[1], Olga D. Jarosinska[1], Anna Akhmanova[3], Christine A. Richardson[8], Maarten Altelaar[4], Rudolf E. Leube[2], João J. Ramalho[1,9]*, and Mike Boxem[1]*

1 – Developmental Biology, Institute of Biodynamics and Biocomplexity, Department of Biology, Faculty of Science, Utrecht University, Padualaan 8, 3584 CH, Utrecht, The Netherlands

2 – Institute of Molecular and Cellular Anatomy, RWTH Aachen University, 52074 Aachen, Germany

3 – Cell Biology, Neurobiology and Biophysics, Institute of Biodynamics and Biocomplexity, Department of Biology, Faculty of Science, Utrecht University, Padualaan 8, 3584 CH, Utrecht, The Netherlands

4 – Biomolecular Mass Spectrometry and Proteomics, Bijvoet Center for Biomolecular Research and Utrecht Institute for Pharmaceutical Sciences, Utrecht University, Padualaan 8, 3584 CH, Utrecht, The Netherlands

5 – Present address: Philochem AG, Libernstrasse 3, CH-8112 Otelfingen, Switzerland

6 – Molecular Cancer Research, Center for Molecular Medicine, University Medical Center Utrecht, Utrecht University, The Netherlands

7 – Oncode Institute, The Netherlands

8 – Department of Biosciences, Durham University, United Kingdom.

9 – Present address: Laboratory of Biochemistry, Wageningen University & Research, Stippeneng 4, 6708 WE, Wageningen, The Netherlands

* Equal contribution

Correspondence: m.boxem@uu.nl

Keywords

Epithelial tube, intermediate filaments, protein aggregation, intestine, *C. elegans*, BUBL-1, C9orf16

Summary

We identify BUBL-1 as an evolutionary conserved regulator of lumen morphology in the *C. elegans* intestine. Loss of *bubl-1* causes intermediate filament network reorganization that induces severe apical morphology defects. We also identify C9orf16 as the mammalian ortholog, which can compensate for the loss of BUBL-1 in *C. elegans*.

Abstract

Epithelial tubes are essential components of metazoan organ systems that control the flow of fluids and the exchange of materials between body compartments and the outside environment. The size and shape of the central lumen confer important characteristics to tubular organs and need to be carefully controlled. Here, we identify the small coiled-coil protein BUBL-1 as a regulator of lumen morphology in the *C. elegans* intestine. Loss of BUBL-1 causes the formation of bubble-shaped invaginations of the apical membrane into the cytoplasm of intestinal cells, and abnormal aggregation of the subapical intermediate filament (IF) network. BUBL-1 interacts with IF proteins and localizes to the IF network in an IF-dependent manner. The appearance of invaginations is a result of the abnormal IF aggregation, indicating a direct role for the IF network in maintaining lumen homeostasis. Finally, we identify C9orf16 as the likely mammalian ortholog of BUBL-1. When expressed in the *C. elegans* intestine, C9orf16 recapitulates the localization pattern of BUBL-1 and can compensate for the loss of BUBL-1. In mouse intestinal organoids, C9orf16 localizes subapically, together with the IF protein keratin 8. Our results therefore may have implications for understanding the role of IFs in regulating epithelial tube morphology in mammals.

Introduction

Epithelial and endothelial tubes are fundamental building units of many organs, including the digestive tract, vascular system, kidney, and lung. Tubular organs are essential for the transport of nutrients, waste products, gases, and ions across large distances. Furthermore, epithelial tubes function as a protective barrier to the outside environment. Tubes consist of a central lumen bounded by the apical domains of one or more epithelial or endothelial cells, and are remarkably varied in size, complexity and mechanism of development (Iruela-Arispe and Beitel, 2013; Lubarsky and Krasnow, 2003; Sigurbjörnsdóttir et al., 2014). The size and shape of the central lumen are precisely controlled, as they confer important biophysical and biochemical properties to biological tubes. Lumen morphology can be very stable, but can also be highly plastic during tissue growth or when subjected to mechanical stimuli or stress (Iruela-Arispe and Davis, 2009; Stutz et al., 2015; Sundaram and Buechner, 2016). The importance of mechanisms that control lumen morphology is highlighted by common pathologies that are characterized by altered lumen architecture, including polycystic kidney disease, cystic fibrosis, and inflammatory bowel disease (Bergmann et al., 2018; Cutting, 2015; Ramos and Papadakis, 2019; Schelling, 2016). The *Caenorhabditis elegans* intestine provides a simple model to study the regulation of lumen morphology. The *C. elegans* intestine is a tube composed of 20 cells arranged in nine segments surrounding a central lumen (Fig. 1A) (Sulston et al., 1983; Leung et al., 1999). Specialized cell-cell junctions at the lateral membrane, known as *C. elegans* apical junctions (CeAJ), keep neighboring cells tightly adherent, ensuring integrity of the epithelium and impermeability of the lumen (Pasti and Labouesse, 2014). The intestinal cells are born during embryogenesis and do not divide or renew during larval development or in adulthood. They are polarized along an apicobasal axis and resemble mammalian enterocytes at the ultrastructural level (Coch and Leube, 2016). The lumen forming apical surface of both cell types is covered by microvilli that contain bundled actin filaments, and are supported by the subapical actin-rich terminal web (Leung et al., 1999; Bossinger et al., 2004). The luminal surface is further supported by an intermediate-filament (IF) rich fibrous sheet that directly underlies — and is likely connected to — the terminal web. The *C. elegans* IF network forms a particularly electron-dense structure anchored at the lateral cell junctions that is known as the 'endotube' (Bossinger et al., 2004; Coch and Leube, 2016; Munn and Greenwood, 1984).

Cytoplasmic IF proteins form resilient and flexible networks that mediate the mechanical properties of cells and tissues and contribute to a diverse range of processes including organelle positioning, intracellular trafficking, and cell motility (Coulombe and Wong, 2004; Etienne-Manneville, 2018). In tubular epithelia, subapical IF networks are ideally positioned to contribute to the regulation of lumen morphology and functioning. Indeed, intestinal IF networks have essential roles in epithelial polarization, maintenance of lumen morphology, and protection from environmental stresses (Etienne-Manneville, 2018; Geisler and Leube, 2016; Salas et al., 2016; Sanghvi-Shah and Weber, 2017; Toivola et al., 2010). In the *C. elegans* intestine, loss of IF subunits, or of the intermediate filament organizers IFO-1 and SMA-5, can result in morphological abnormalities of the lumen and increased susceptibility to microbial, osmotic, and oxidative stresses (Carberry et al., 2012; Geisler et al., 2016, 2019, 2020).

Here, we report the identification of an evolutionary conserved regulator of intestinal tube morphology and IF organization we term *bubl-1,* for bulges budding from the intestinal lumen. *bubl-1* mutants are characterized by the presence of large invaginations of the apical lumen into the cytoplasm of intestinal cells. The BUBL-1 protein physically interacts with IF proteins and localizes to the endotube in an IF-dependent manner. Loss of BUBL-1 causes defects in the organization of the intestinal IF network, which aggregates into thick bundles at the neck of cytoplasmic invaginations. Surprisingly, the invagination phenotype of *bubl-1* mutants is rescued by removal of the IF network. This indicates that the cytoplasmic invaginations are the result of the aggregated IF network state caused by loss of *bubl-1*. We identified the protein C9orf16 as the likely mammalian ortholog of BUBL-1, based on sequence similarity, overlap in protein interaction partners,

and the ability of C9orf16 to partially substitute for BUBL-1 functioning in the *C. elegans* intestine. Our findings provide further evidence that the subapical IF network plays an active role in regulating the morphology of tubular epithelia, while the structural and functional conservation from *C. elegans* to humans provides a model for studying IF modulation *in vivo*.

Results

Loss of bubl-1 causes cytoplasmic invaginations of the intestinal apical membrane

To investigate the mechanisms that regulate intestinal lumen morphology, we performed a genetic screen in *C. elegans* for mutants with lumen morphology defects. We mutagenized a strain expressing the apical membrane protein ERM-1 endogenously fused to GFP, and screened for viable F2 progeny with aberrations in lumen morphology (Fig. 1A–D). We identified two independent mutants (*mib41* and *mib42)* with dramatic bubble-shaped protrusions of the apical plasma membrane into the cytoplasm of the intestinal cells (Fig. 1C, D). Complementation analysis indicated that *mib41* and *mib42* affect two independent loci. We determined the genomic regions of interest by single nucleotide polymorphism (SNP) mapping (Davis et al., 2005), and identified candidate causative mutations using the sibling subtraction method for mapping by whole-genome sequencing (Joseph et al., 2018). We obtained a single cluster of candidate mutations for each mutant allele on opposite arms of the X chromosome, consistent with the SNP mapping data.

Only one among the candidate *mib41* mutations was predicted to exert a detrimental effect on protein function, by inducing a missense mutation within the *sma-5* open reading frame (ORF) (C370T in *sma-5a*). At the protein level, this mutation results in an arginine to tryptophan substitution in the kinase domain of all predicted isoforms (Arg124Trp in SMA-5a) (Fig. S1A). SMA-5 is a member of the conserved mitogen-activated protein kinase (MAPK) family that is required for intestinal lumen morphogenesis (Geisler et al., 2016). *sma-5* mutations induce a lumen invagination phenotype similar to *mib41* mutants (Geisler et al., 2016) and the strong loss of function *sma-5(n678)* allele (Watanabe et al., 2005) failed to complement *mib41*. Together, these data show that *mib41* is a novel *sma-5* allele.

The *mib42* sequencing data also yielded a single potentially deleterious mutation within a predicted ORF: a C to T transition resulting in an early stop at the fifth codon of the uncharacterized gene *C15C7.5* (Fig. 1E, F). We used several strategies to confirm that loss of *C15C7.5* function was responsible for the intestinal lumen morphology defects in *mib42* animals. First, *C15C7.5* RNA interference (RNAi) feeding experiments in ERM-1::GFP animals revealed apical membrane invaginations similar to those observed in the mutant (Fig. S1B). Second, transgenic expression of *GFP::C15C7.5* from the intestinal specific *vha-6* promoter fully rescued the invagination phenotype of *mib42* animals (Fig. S1C). Lastly, we generated a *C15C7.5* null allele, *mib70*, by removing the entire *C15C7.5* coding sequence using CRISPR/Cas9 engineering. The *mib70* deletion, from here on referred to as *C15C7.5(null),* caused cytoplasmic invaginations (Fig. S1D) and was unable to complement *mib42*. Both *C15C7.5(mib42)* and *C15C7.5(null)* animals are homozygous viable, but animals appear somewhat sick and display a slight clear phenotype. The invagination phenotype observed in *C15C7.5(null)* animals was more severe than in *mib42* mutants (Fig. 1G). This data indicates that *mib42* is a partial loss-of-function mutation in the *C15C7.5* gene, and that C15C7.5 controls intestinal lumen morphology. We have named the *C15C7.5* gene *bubl-1* for <u>bu</u>lges <u>b</u>udding from the intestinal <u>l</u>umen.

We next examined the intestinal cytoplasmic invaginations in more detail. In *bubl-1(null)* animals, invaginations were visible from hatching onwards, and the number of invaginations per intestinal ring remained constant throughout development (Fig. 1G, H). Invagination width correlated with intestinal cell width, and in late larval and adult stages invaginations had an elongated appearance (Fig. 1I). The *bubl-1* invaginations

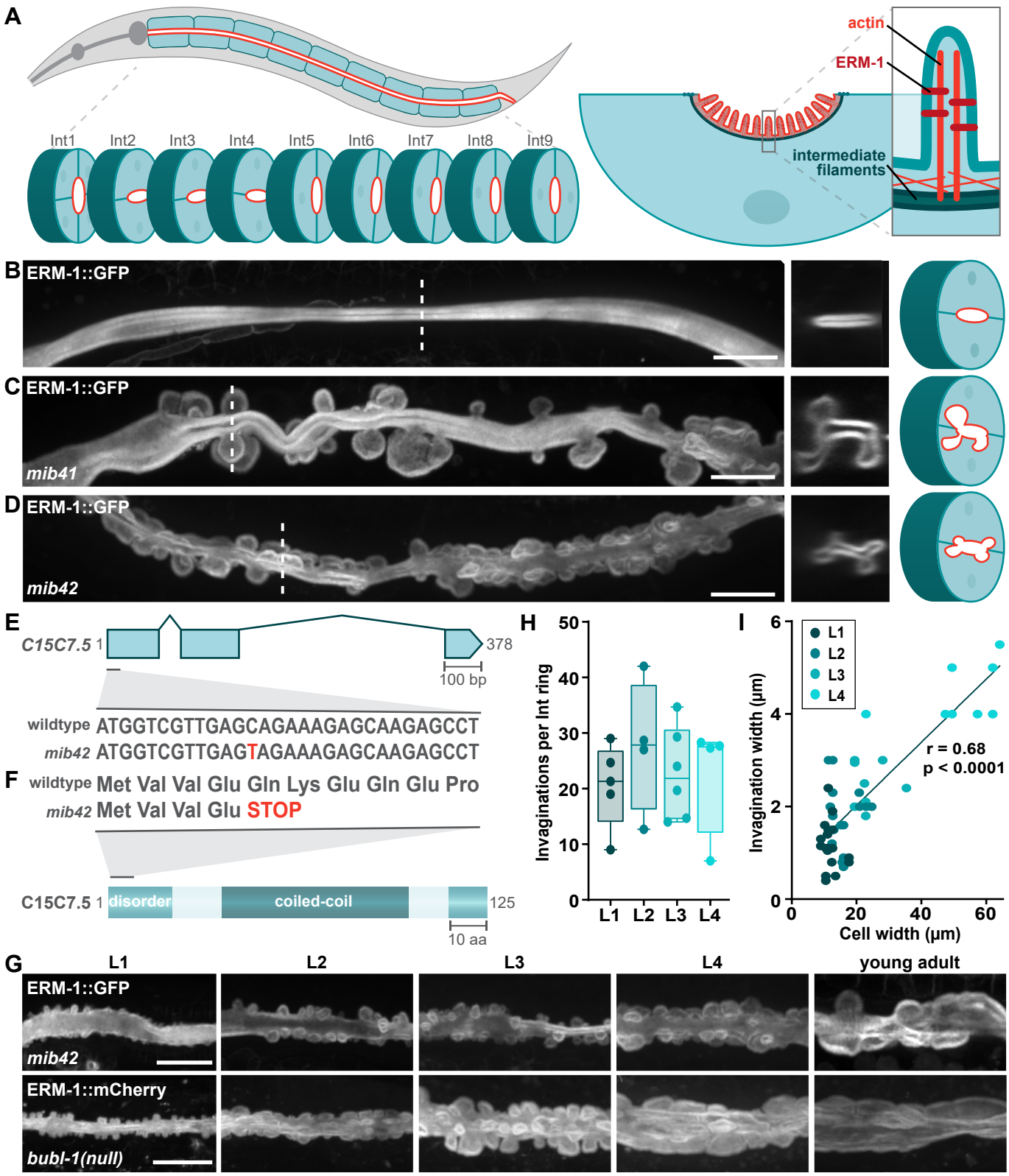

Figure 1 – The intestines of *mib41* and *mib42* mutants show cytoplasmic invaginations. (**A**) Schematic representation of the *C. elegans* intestine (left) and the subcellular intestinal localization of proteins and cytoskeletal elements relevant for this study (right). (**B–D**) Intestinal apical membrane morphology in L4 animals visualized with an endogenous ERM-1::GFP reporter. Dotted lines in left panels indicate position of cross-section views. Schematics depict cross-section with apical membrane in red. Unless otherwise indicated, in this and all other figures, images were acquired using spinning-disk confocal microscopy, lateral views are maximum intensity projections, anterior is to the left, and scale bars indicate 10 µm. (**E, F**) Genomic structure of the *C15C7.5* gene (E) and representation of the C15C7.5 protein with predicted domains (F). Boxes in the genomic structure correspond to exons while lines represent introns. Part of the DNA and amino acid sequence is shown for both the wild-type and *mib42* mutant allele. (**G**) Progression of *mib42* and *bubl-1(null)* invagination phenotype throughout development visualized by endogenous

ERM-1::GFP and ERM-1::mCherry reporters, respectively. (**H**) Quantification of number of invaginations per intestinal ring, per larval stage in *bubl-1(null)* animals. Each data point represents the average number of invaginations per intestinal ring in one animal. Data is presented as median ± interquartile range. Differences are not significant (Kruskal-Wallis followed by Dunn's multiple comparisons test; $P > 0.99$). (**I**) Correlation between cell and invagination width in *bubl-1(null)* animals, color coded per larval stage. Linear regression is shown for all data points combined. Data is analyzed with nonparametric Spearman correlation; $r = 0.6824$, $P < 0.0001$.

were spread uniformly along the length of the intestine (Fig. 1D, G). However, in cross section, invaginations seemed to preferentially localize at the vertices of the ellipse shaped lumen, in proximity to cell junctions. This was particularly noticeable in *mib42* animals, which have fewer invaginations than the *bubl-1(null)* mutant (Fig. 1D). To confirm this, we visualized invaginations in a *bubl-1(mib42)* strain expressing the junctional protein DLG-1 endogenously tagged with mCherry. Indeed, invaginations occurred in proximity to cell junctions (Fig. S1E–H).

Finally, we assessed whether invaginations are contiguous with the lumen by feeding animals with a membrane impermeable Texas Red-dextran conjugate. In wild-type animals, Texas Red signal filled the lumen and was enclosed by the ERM-1::GFP-labelled apical membrane (Fig. S1I). Similarly, in *bubl-1(mib42)* animals, all invaginations contained Texas Red signal, indicating that they are contiguous with the lumen. Moreover, we never observed internalized invaginations or presence of Texas Red signal in the cytoplasm of intestinal cells, indicating that the invaginations are stable and do not internalize.

BUBL-1 is a small coiled-coil protein that localizes dynamically to intermediate filament-rich structures

bubl-1 is predicted to encode a single protein isoform of just 125 amino acids. A central coiled-coil domain (aa 39–102) is the only recognizable feature, with the remainder of the protein predicted to be intrinsically disordered (Fig. 1F). To investigate the function of BUBL-1 in intestinal lumen morphogenesis, we first analyzed its expression pattern and subcellular localization. We used CRISPR/Cas9 engineering to introduce the GFP coding sequence immediately upstream of the *bubl-1* start codon. Homozygous knock-in animals expressing GFP::BUBL-1 do not show obvious developmental or intestinal lumen defects, demonstrating that the fusion protein is functional. We also generated a C-terminally mKate2 tagged variant. However, homozygous *bubl-1::mKate2* animals displayed the intestinal cytoplasmic invagination phenotype, indicating a non-functional protein fusion. We therefore used the N-terminal GFP fusion for our experiments.

BUBL-1 was first apparent at the comma stage of embryonic development, at the apical domain of intestinal cells (Fig. 2A). In subsequent embryonic stages, BUBL-1 became visible in the hypodermis and pharynx as well. During larval and adult stages, we detected BUBL-1 in many epithelial tissues including the pharynx, intestine, excretory canal, hypodermis, vulva, and uterine seam (Fig. 2B). In each of these tissues the distribution of BUBL-1 was similar to previously reported distribution of intermediate filament proteins. In the marginal cells of the pharynx, we observed a pattern of short radial filaments, reminiscent of the IF containing tonofilaments (Fig. 2Bi) (Karabinos et al., 2003). In the excretory canal, BUBL-1 localization was similar to that of the intermediate filament proteins IFA-4, IFB-1, and EXC-2/IFC-2 (Fig. 2Bii) (Al-Hashimi et al., 2018; Khan et al., 2019). In the hypodermis, we observed a pattern strongly resembling that of intermediate filaments in the *C. elegans* hemidesmosomes (Fig. 2Biii) (Pasti and Labouesse, 2014; Woo et al., 2004). We also observed expression of BUBL-1 in the uterine seam and vulva (Fig. 2Biv), as previously reported for IFA-1, MUA-6/IFA-2, IFB-1 and EXC-2/IFC-2 (Al-Hashimi et al., 2018; Hapiak et al., 2003; Karabinos et al., 2003; Williams et al., 2015; Woo et al., 2004).

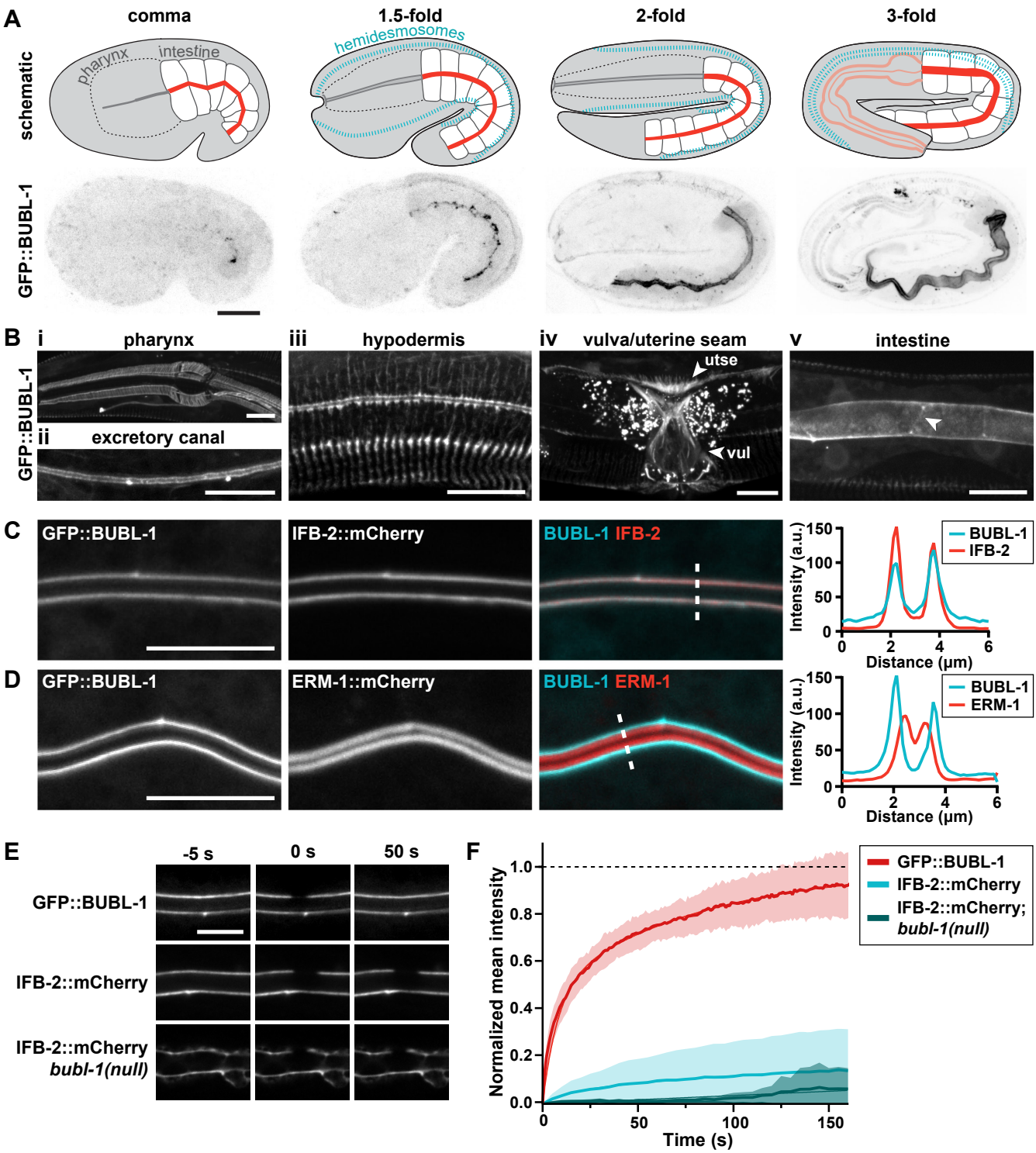

Figure 2 – BUBL-1 localizes dynamically to intermediate filament-rich structures. (**A, B**) Distribution of the endogenous GFP::BUBL-1 reporter during late embryonic development (A) and in different tissues in L3 (intestine) and L4 larvae (pharynx and excretory canal images), and young adults (hypodermis and vulva images) (B). (**C, D**) Distribution of GFP::BUBL-1 compared with ERM-1::mCherry (C) and IFB-2::mCherry (D) at the apical domain of intestinal cells of L3 larvae. Dashed lines indicate sites of intensity profiles shown in the graphs to the right. (**E, F**) Stills from time-lapse movies (E) and FRAP curves (F) corresponding to bleached portions of the apical domain in larval intestines. Time-lapse data was acquired at 1 s intervals for GFP::BUBL-1 (n = 7) and 5 s intervals for IFB-2::mCherry (WT: n = 6, *bubl-1(null)*: n = 5). Thin lines and shading represent the mean ± SD. GFP::BUBL-1 plateau = 0.995, fast half-time = 5.45 s, slow half-time = 55.72, R^2 = 0.998; IFB-2::mCherry plateau = 0.188, fast half-time = 8.8 s, slow half-time = 97.32, R^2 = 0.998. For IFB-2::mCherry in a *bubl-1(null)* background, R^2 = 0.817 and no plateau or half-times could be accurately determined.

In the intestine, BUBL-1 localized subapically with apparent accumulation around cell junctions (Fig. 2Bv). This localization pattern corresponds to the distribution of the endotube (Bossinger et al., 2004). To confirm that BUBL-1 resides at the endotube, we generated an endogenous mCherry fusion of the intestinal intermediate filament protein IFB-2. We then analyzed the localization of BUBL-1 relative to IFB-2 and to ERM-1, which localizes apically at microvilli (Bidaud-Meynard et al., 2019; Ramalho et al., 2020). Consistent with localization to the endotube, we found that BUBL-1 colocalizes with IFB-2, basal to ERM-1 (Fig. 2C, D). To determine if BUBL-1 stably associates with the IF network, we performed fluorescence after photobleaching (FRAP) experiments. IFB-2 fluorescence recovered only ~15% in 150 seconds (Fig. 2E, F). Similar slow recovery was previously reported for IFA-1 and IFB-1 in the pharynx (Karabinos et al., 2003). In contrast, BUBL-1 recovered roughly 90% within the same period, indicating that BUBL-1 localizes to the IF network in a dynamic fashion. Taken together, these results indicate that BUBL-1 is a dynamic component of the endotube in intestinal cells.

BUBL-1 requires an IF network for its localization and interacts with IF proteins

As BUBL-1 localizes together with IF proteins, we next determined whether the apical localization of BUBL-1 depends on IFs. The *C. elegans* intestine expresses six cytoplasmic IF proteins, all of which localize almost exclusively to the endotube (Bossinger et al., 2004; Geisler et al., 2020; Karabinos et al., 2002, 2004). We used RNAi feeding to knock down the individual intestinal IF proteins in a strain that endogenously expresses GFP::BUBL-1 and ERM-1::mCherry. We observed significant reduction in apical BUBL-1 upon knockdown of IFB-2, IFD-1, IFD-2, or IFP-1 (Fig. 3A, B). In *ifb-2(RNAi)* animals, the loss of BUBL-1 from the apical cortex was most striking. IFB-2 is an essential component of the apical intestinal IF network, and loss of IFB-2 results in a complete absence of the endotube (Geisler et al., 2019, 2020). Therefore, the strong reduction in apical BUBL-1 may be due to an additive effect of losing the localization of all cytoplasmic IFs. These data demonstrate that BUBL-1 requires the presence of an IF network for its apical localization. We also examined the localization of BUBL-1 in the excretory canal of *ifc-2(RNAi)* animals, as IFC-2 has been shown to be important for the structure of this tissue (Al-Hashimi et al., 2018). We observed a marked relocalization of BUBL-1 from the apical cortex to the cytoplasm and basal membrane, which suggests that dependency on IFs is a general aspect of BUBL-1 localization (Fig. 3C).

The reliance on an intact IF network for BUBL-1 to properly localize might originate from a physical interaction with IF proteins. To identify candidate interacting proteins, we performed affinity purification of GFP::BUBL-1 from mixed-stage *C. elegans* cultures, followed by mass spectrometry analysis. The highest-ranking proteins we identified included all intestinal IF proteins except IFP-1, as well as all proteins of the IFA/IFB system (IFA-1, 2, 3, 4 and IFB-1) (Fig. 3D). After IFB-1, the two most highly ranked candidate interactors were VHA-9 and VHA-14, the *C. elegans* orthologs of subunits F and D of the stalk region of the highly conserved vacuolar ATPase (V-ATPase) V1 domain, which localizes to the luminal domain of the intestine (Ji et al., 2006). Other high-confidence hits included various hemidesmosome components (i.e. VAB-10, LET-805, PAT-12 and MUP-4) and actin-interacting proteins like the crosslinker FLN-2, and the myosins UNC-15 and MYO-2. Altogether, our mass spectrometry data suggests a physical interaction between BUBL-1 and IFs and provides cues for future investigations into the activities of BUBL-1.

To further confirm the dependency of BUBL-1 localization on IFs, we examined the effects of inactivation of known regulators of intermediate filament organization on BUBL-1. In addition to *sma-5,* loss of *ifo-1, act-5,* and *let-413* have all been reported to disrupt IFB-2 distribution in the *C. elegans* intestine (Bossinger et al., 2004; Carberry et al., 2012; Estes et al., 2011; Stutz et al., 2015). IFO-1 localizes to the adluminal domain, together with but independently from IFB-2, and its depletion causes aggregation of IFs at cell junctions as well as in the cytoplasm (Carberry et al., 2012). Reducing the levels of the intestinal actin ACT-5 causes gaps in the normally uninterrupted IFB-2 network, and has been reported to result in the appearance of cyto-

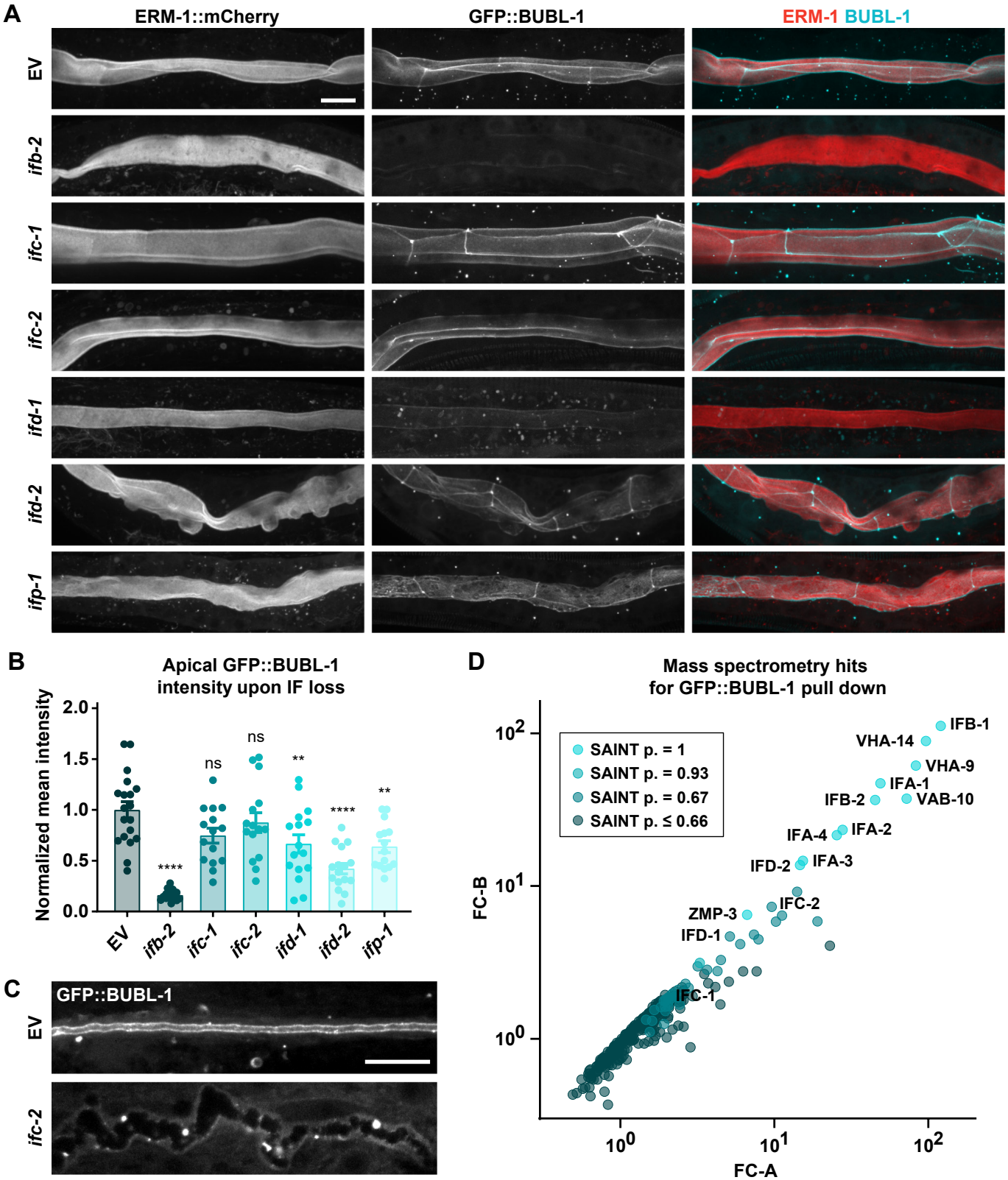

Figure 3 – BUBL-1 requires intermediate filaments for its apical localization in the intestine. (**A**) Intestinal GFP::BUBL-1 distribution and apical membrane morphology, visualized by ERM-1::mCherry, upon RNAi knockdown of targets indicated to the left. EV = empty vector. (**B**) Quantification of GFP::BUBL-1 levels at the intestinal apical domain of larvae subjected to RNAi knockdown of targets indicated at the X-axis. Each data point represents the average of six or eight measurements in a single animal (n = 19, 17, 15, 15, 16, 16, and 15 animals, respectively). Larvae were L2–L4 stage. Data is presented as mean ± SEM and analyzed with ordinary one-way ANOVA followed by Dunnett's multiple comparisons test; ns = P > 0.05, ** = P < 0.005, **** = P < 0.0001. (**C**) GFP::BUBL-1 distribution in the excretory canal upon RNAi knockdown of targets indicated on the left. EV = empty vector. (**D**) Mass spectrometry hits for GFP::BUBL-1 pull down plotted as correlation between fold-change (FC) score A and more stringent FC score B. Data points are color coded for different SAINT probability scores.

plasmic invaginations (Estes et al., 2011; Stutz et al., 2015). Finally, depletion of LET-413 causes aberrant localization of IFB-2 to the lateral and basal domains of intestinal cells in the embryo (Bossinger et al., 2004). We depleted each protein by RNAi in a strain expressing either ERM-1::mCherry (to visualize lumen morphology) or IFB-2::mCherry, together with GFP::BUBL-1. The phenotypes we observed matched published reports, though RNAi for *act-5* caused more severe IFB-2 defects, with invaginations only visible in a small subset of animals (Fig. 4A–C). Importantly, in each case the localization of BUBL-1 followed the localization pattern of IFB-2, confirming that BUBL-1 colocalizes with IFs.

Interestingly, in *sma-5(RNAi)* intestines, we observed a significant reduction in cortical enrichment of BUBL-1 (Fig. 4D). This suggests that *sma-5* acts upstream of *bubl-1*. To determine if *sma-5* and *bubl-1* act in a linear pathway, we performed *sma-5* RNAi in a *bubl-1(null)* background. The resulting animals displayed more severe intestinal abnormalities than either *sma-5(RNAi)* or *bubl-1(null)* alone (Fig. 4E). Thus, while *sma-5* may act in part through *bubl-1*, both genes act at least partially independent.

Collectively, our results indicate that the subcellular distribution of BUBL-1 depends physically on the presence of intermediate filaments.

Loss of bubl-1 compromises the integrity of the IF network

Apical domain invaginations in *sma-5* mutants were previously linked to defects in IF organization by fluorescence and electron microscopy (Geisler et al., 2016). Unlike the uniform electron-dense endotube surrounding the lumen in wild-type animals, endotube thickness in *sma-5* mutant animals is highly variable (Geisler et al., 2016). The phenotypic similarities between *sma-5* and *bubl-1* mutants, as well as the localization of BUBL-1 to IF-rich structures, led us to hypothesize that apical domain invaginations in *bubl-1* mutant animals were similarly associated with defects in intestinal IF organization. To address this, we analyzed the distribution of three different intestinal IF proteins in *bubl-1(null)* animals: IFB-2, IFC-2, and IFD-2. For IFC-2, we used an existing CRISPR knock-in line expressing IFC-2a/e fused to the yellow fluorescent protein (IFC-2a/e::YFP) (Geisler et al., 2019, 2020). For IFD-2 we generated an endogenous *gfp::ifd-2* locus using CRISPR/Cas9.

In control animals, IFB-2 and IFC-2 were distributed evenly along the adluminal domain (Fig. 5A, C). Both proteins were also enriched at cell junctions, with IFC-2 showing stronger junctional enrichment than IFB-2. These localization patterns match prior observations (Hüsken et al., 2008; Carberry et al., 2012; Geisler et al., 2016, 2020). In contrast to IFB-2 and IFC-2, IFD-2 showed a clearly punctate localization pattern and was excluded from cell junctions (Fig. 5E, S2A). The distinct localization of IFD-2 indicates functional specialization within the IF network.

Upon loss of *bubl-1*, all three IF proteins retained their subapical localization, but formed a network of cables or bundles of increased fluorescence intensity, surrounding protrusions into the cytoplasm with reduced fluorescence signal (Fig. 5B, D, F). IFD-2 lost its punctate localization pattern, instead localizing to cable-like structures (Fig. 5F). To investigate the stability of IFs within the aggregated bundles, we performed FRAP on IFB-2::mCherry in *bubl-1(null)* animals. IFB-2 showed very little fluorescence recovery, appearing if anything even more stable than in control animals (Fig. 2E, F). Together these data indicate that BUBL-1 is required for the integrity of the IF network but not for IF recruitment to the subapical cortex.

To investigate whether BUBL-1 is required for IF network integrity throughout development or only during a critical time in intestinal development, we made use of the auxin-inducible degradation (AID) system. The AID system enables targeted degradation of AID-degron tagged proteins through expression of the

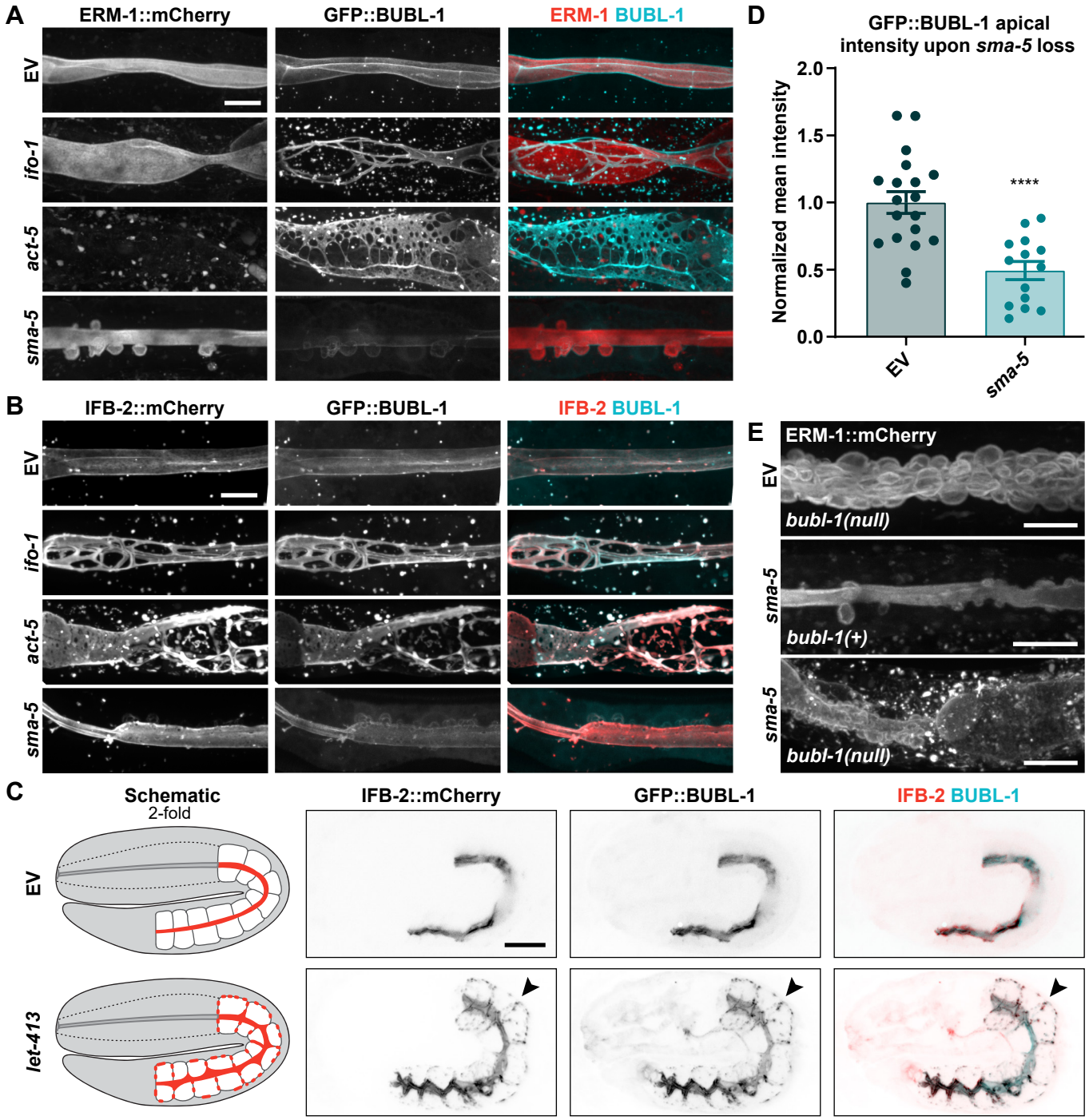

Figure 4 – BUBL-1 co-localizes with disrupted or mislocalized IFs. (**A**) Intestinal GFP::BUBL-1 distribution and apical membrane morphology, visualized by ERM-1::mCherry, after RNAi knockdown of targets indicated on the left. EV = empty vector control. Same EV control is shown as in Fig. 3A since data is from a single experiment. (**B, C**) GFP::BUBL-1 and IFB-2::mCherry distribution in L2 (*act-5*), L3 (*ifo-1, sma-5*) and L4 (EV) larvae (B) and 2-fold embryos (C) after RNAi knockdown of targets indicated on the left. (**D**) Quantification of GFP::BUBL-1 levels at the intestinal apical domain of L3 and L4 larvae subjected to RNAi knockdown of *sma-5*. Each data point represents the average of six or eight measurements in a single animal (n = 19 and 14 animals, respectively). Data is presented as mean ± SEM and analyzed with ordinary one-way ANOVA followed by Dunnett's multiple comparisons test; **** = P < 0.0001. EV control data is same as in Fig. 3B. (**E**) Apical membrane morphology, visualized by ERM-1::mCherry, after RNAi knockdown of targets indicated on the left in *bubl-1(+)* or *bubl-1(null)* background.

plant-derived auxin-dependent E3 ubiquitin ligase specificity factor TIR1 (Nishimura et al., 2009; Zhang et al., 2015). We used CRISPR/Cas9 genome engineering to tag BUBL-1 N-terminally with GFP and the AID-degron and expressed TIR1 from the intestine-specific *elt-2* promoter. Within 1 hour of addition of auxin to L1-stage animals, GFP::AID::BUBL-1 was no longer detectable at the luminal domain of the intestine (Fig. S2B). We then crossed the GFP::AID::BUBL-1 line with a line expressing IFB-2::mCherry and ERM-1::GFP to examine intestinal morphology over time. We added auxin to late L1 stage or early L4 stage animals and imaged the intestinal lumen after 24 h and 48 h (Fig. S2C). Irrespective of the starting time point, approximately half of the animals had developed invaginations after 24 hours of auxin treatment (Fig. S2D, 48-hour developmental timepoint). The remainder showed small 'holes' in the normally contiguous IFB-2::mCherry fluorescent pattern (Fig. S2E). Eventually, all animals treated with auxin from L1 developed cytoplasmic invaginations (Fig. S2D, 72-hour developmental timepoint). These data show that *bubl-1* is required to maintain the integrity of the IF network throughout development and further indicate that an intact IF network is essential for homeostasis of the intestinal lumen.

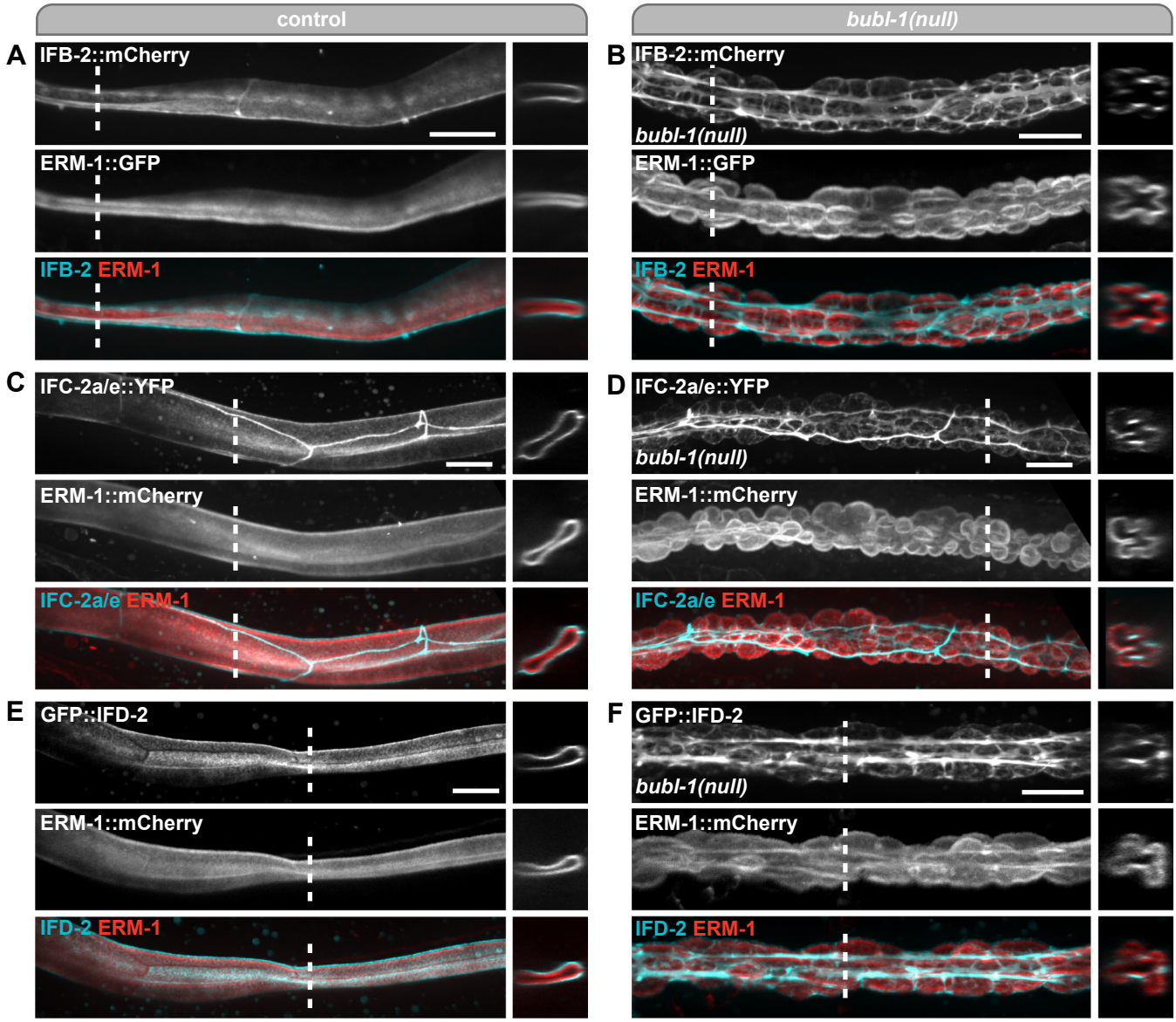

Figure 5 – Loss of *bubl-1* compromises the integrity of the intermediate filament network. (**A–F**) Organization of the intestinal IF network visualized with IFB-2::mCherry (A, B), IFC-2a/e::YFP (C, D) or GFP::IFD-2 (E, F) in control (A, C, E) or *bubl-1(null)* (B, D, F) animals. Large panels are lateral views and small panels are cross-sections at the site indicated by the dashed lines.

In addition to the IF network, the apical domain of the intestine is highly enriched in actin, which is present both in microvilli and the supporting terminal web. To investigate if the actin cytoskeleton is disrupted, we examined the localization of the intestinal actin ACT-5 in *bubl-1(null)* animals, using a YFP::ACT-5 transgene (Bossinger et al., 2004). In *bubl-1* animals, ACT-5 smoothly decorated the surface of the cytoplasmic invaginations and was not enriched in bundles or cables (Fig. S2F,G). Thus, loss of BUBL-1 function appears to specifically affect the IF network and not the terminal web or microvillar actin. We also investigated whether the loss of *bubl-1* disrupted the overall polarization of the intestinal cells. Inactivation of *bubl-1* by RNAi did not affect the basolateral localization of an endogenous LET-413/Scribble::mCherry marker, nor the apical localization of an endogenous PAR-6::GFP marker (Fig. S2H,I). Thus, the effects of *bubl-1* on the IF network are not due to a loss of intestinal polarity. Moreover, as invaginations are coated with PAR-6, ERM-1, and ACT-5, the formation of invaginations is not accompanied by a loss of apical identity.

To confirm loss of IF network integrity in *bubl-1* mutants and analyze intestinal morphology at the ultrastructural level, we performed electron microscopy on *bubl-1(null)* mutants. Previously, it was shown that in *sma-5* mutant intestines, the endotube is lost or diminished at sites of invagination and thickened around invagination necks (Geisler et al., 2016). In *bubl-1(null)* animals, the endotube appears to be similarly affected as in *sma-5* mutants. Endotube remnants appeared as aggregated electron-dense material, and no longer displayed the characteristic two lines of electron-dense material defining the endotube in wild-type intestines (Fig. 6, compare A vs. B or C vs. D). Nevertheless, as in wild-type animals, aggregated endotube material in *bubl-1(null)* intestines still maintained a characteristic distance from the apical membrane, consistent with the continued presence of the subapical terminal web (Fig. 6A, B, inlays). Finally, the electron microscopy images revealed that microvilli are still abundant in invaginations. These data suggests that the presence of BUBL-1 and a fully assembled endotube are not required for microvilli formation, which is consistent with previous data on *ifb-2* null mutants (Geisler et al., 2019).

Taken together, the EM and light microscopy observations demonstrate that the intestinal IF network collapses and aggregates into stable bundles upon loss of BUBL-1, without affecting other aspects of intestinal epithelial polarity or the actin cytoskeleton.

Apical IF aggregation drives cytoplasmic invaginations

We next sought to better understand the relationship between the cytoplasmic invaginations and collapsed IF network observed in *bubl-1* mutants. If invaginations are a consequence of the IF network collapse, more direct disruption of the IF network might be expected to similarly cause invaginations. Indeed, *ifd-2(RNAi)* induced cytoplasmic invaginations, though with much lower penetrance and severity than *bubl-1* mutants (Fig. 3A). A recent study similarly showed that *ifd-2* knockout causes cytoplasmic invaginations, while retaining apical IFB-2 and IFC-2 localization (Geisler et al., 2020). We also observed that knockdown of *ifp-1* causes an irregular apical surface and mildly fragmented BUBL-1 distribution (Fig. 3A). These data indicate that the cytoplasmic invaginations observed in *bubl-1* mutants are caused by defects in the IF network.

Surprisingly, despite the loss of the complete intestinal IF network, *ifb-2* knockout animals have been reported to be overall healthy in appearance, with only mild intestinal lumen morphology defects and increased susceptibility to stresses (Geisler et al., 2020). We also observed an irregular lumen morphology in only a subset of *ifb-2(RNAi)* animals (Fig. 3A, S3A). Importantly, loss of *ifb-2* does not result in cytoplasmic invaginations (Fig. 3A, S3A). This indicates that the invaginations observed in *bubl-1* mutants are due to an altered IF network state. If this is the case, loss of the IF network should suppress the invaginations in *bubl-1* animals. To test this, we generated a double mutant carrying the *bubl-1(null)* allele and the *ifb-2(kc14)* deletion allele (Geisler et al., 2019), expressing ERM-1::mCherry to mark the membrane. Indeed, *ifb-2(kc14)* suppressed the intestinal defects of *bubl-1(null)* (Fig. S3B). The lumen morphology in the double knockout

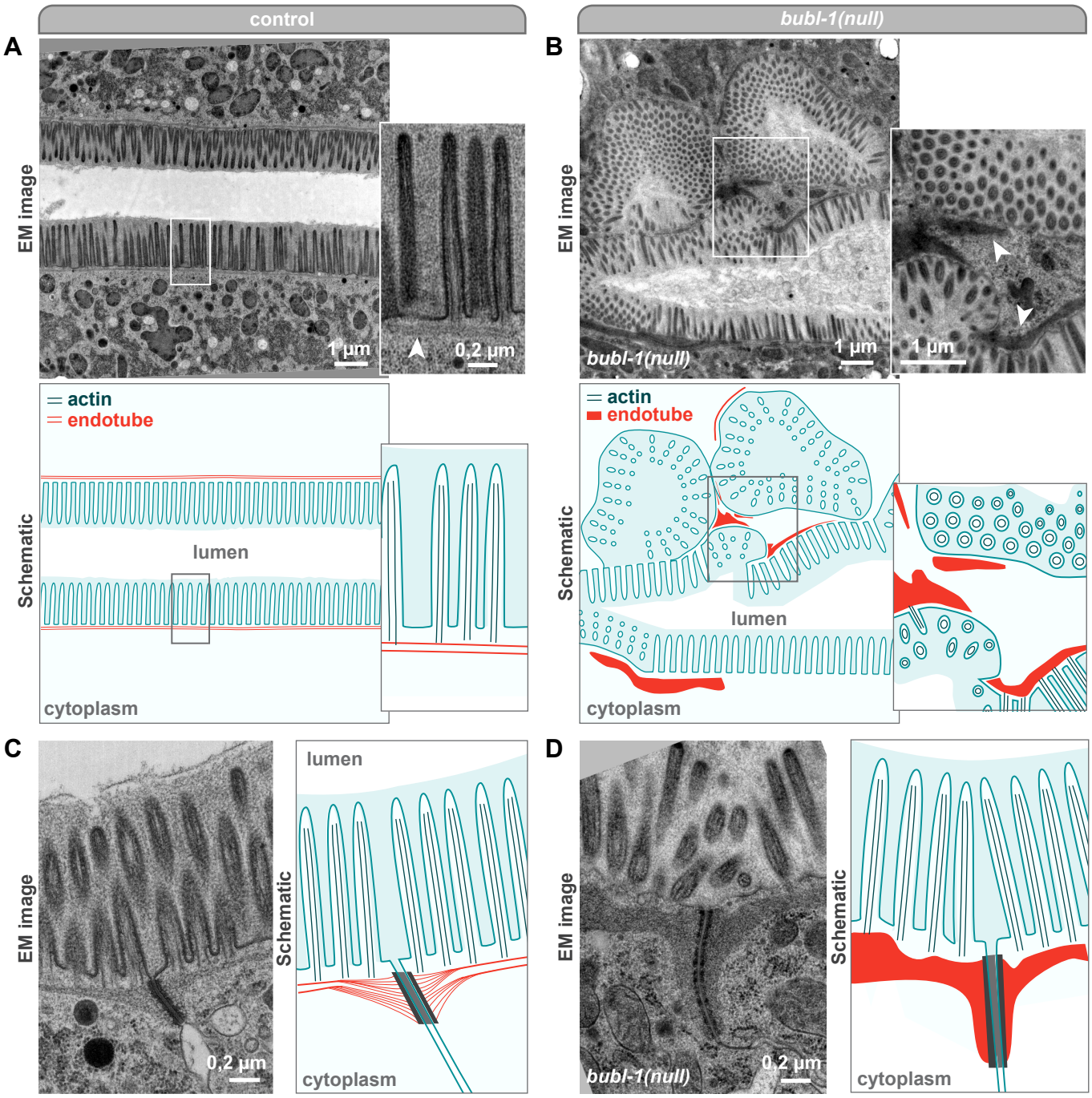

Figure 6 – Loss of *bubl-1* compromises the integrity of the endotube. (**A, B**) Ultrastructure of the apical domain in intestinal cells of *bubl-1(+)* and *bubl-1(null)* adult animals visualized by transmission electron microscopy. Boxed region is shown enlarged and arrowheads point to the endotube. Schematics indicate actin bundles in blue and endotube in red. (**C, D**) Electron microscopy images showing the endotube at apical junctions. Schematics indicate actin bundles in blue, endotube in red, and junction in grey.

appeared identical to that seen for IFB-2 depletion alone in *ifb-2(RNAi)* animals (Fig. 3A) as well as previously published for *ifb-2(kc14)* (Geisler et al., 2020).

In agreement with the fluorescence microscopy data, we did not observe cytoplasmic invaginations by electron microscopy in *ifb-2(kc14); bubl-1(null)* double mutants (Fig. S3C). No endotube was visible, confirming the requirement for IFB-2 in endotube formation. Surprisingly, we did observe occasional small membrane protrusions directed towards the lumen (Fig. S3D), which were also visible by light microscopy in both *ifb-2(kc14); bubl-1(null)* (Fig. S3E) and *ifb-2(RNAi)* animals (Fig. S3Aiii), and are therefore likely to be the result

of IFB-2 depletion alone. Microvillar actin bundles appeared to cluster together at the neck of these small protrusions, forming fan-like structures. One possibility is that, in the absence of the supporting role of the endotube, microvillar actin bundles become linked together, causing the formation of these small extrusions.

Taken together, our data are consistent with a model in which loss of *bubl-1* leads to an altered, pathogenic IF network state that results in cytoplasmic invaginations.

C9orf16 is the mammalian ortholog of BUBL-1

In both *C. elegans* and mammals, intestinal IFs function in mechanical support and protection against stresses. While the IF protein families have diverged between *C. elegans* and mammals (Erber et al., 1998; Weber et al., 1989), it is likely that essential aspects of the regulation of IF networks are conserved. We therefore investigated if BUBL-1 is conserved in mammals. An iterative search using Jackhmmer (Potter et al., 2018) revealed the uncharacterized protein C9orf16 as the only candidate mammalian homolog (E-value 3.8e-16). The 83 aa human C9orf16 protein is predicted to consist of a coiled-coil domain, flanked by intrinsically disordered regions — similar to the predicted structure of BUBL-1 (Fig. 7A). The region between amino acids 27 to 102 in BUBL-1 is most similar to C9orf16, with 26% shared amino acid identity and 48% similarity. A reciprocal Jackhmmer search starting with C9orf16 also identified BUBL-1 as the only *C. elegans* homolog (E-value 8.4e-07). We used the DRSC Integrative Ortholog Prediction Tool v7.1 (Hu et al., 2011) to query multiple orthology prediction databases, but only OrthoDB v9 (Zdobnov et al., 2017) identified C9orf16 and BUBL-1 as candidate orthologs. Nevertheless, given the bi-directional best hit in Jackhmmer and the absence of other candidate orthologs, we consider it likely that BUBL-1 and C9orf16 are evolutionary orthologs.

To investigate if C9orf16 and BUBL-1 are functionally conserved, we generated transgenic animals expressing GFP::C9orf16 in the intestine of *C. elegans* from an extrachromosomal array. C9orf16 showed apical and perinuclear enrichment, resembling the localization pattern of BUBL-1 when similarly expressed from an extrachromosomal array (Fig. 7B). Moreover, as we observed for BUBL-1, the sub-apical localization of C9orf16 was dependent on the presence of an intact IF network (Fig. S4A). To determine if C9orf16 can functionally replace BUBL-1, we examined the effects of mosaic C9orf16 expression in a *bubl-1(null)* background. As expected, *bubl-1(null)* animals not inheriting the transgenic array all showed invaginations from hatching (Fig. 7D). In contrast, in mutant animals that did inherit the transgene, cells expressing C9orf16 did not show invaginations at hatching (Fig. 7C, D). As animals developed, invaginations began to form in all cells, and animals became phenotypically indistinguishable from non-transgenic animals by mid-L1 stage. Thus, expression of C9orf16 delays the invagination phenotype in young larvae. Together, these findings indicate that C9orf16 is a functional homolog of BUBL-1.

We next investigated if the interaction with intermediate filaments is conserved. Keratin 8 (KRT8) is the most common type II keratin IF in simple epithelia, and in enterocytes KRT8 is part of an apical IF network (Schwarz et al., 2015). As KRT8 forms functional heterodimers with KRT18 (Asghar et al., 2015), we investigated if C9orf16 interacts with KRT8/KRT18 by affinity purification from HEK293T cells. Pull-down analysis from HEK293T cell lysates showed that KRT8/KRT18 co-purify with C9orf16 (Fig. 7E). Additionally, multiple high-throughput studies found C9orf16 as an interactor of the type I intestinal keratin KRT20 (Luck et al., 2020; Rolland et al., 2014; Rual et al., 2005). Thus, the interaction with intermediate filaments is conserved between BUBL-1 and C9orf16.

We also performed mass spectrometry analysis on C9orf16 purified from HEK293T cells. The top scoring hit was V-ATPase subunit D (ATP6V1D), the ortholog of *C. elegans* VHA-14 and second highest scoring hit in our

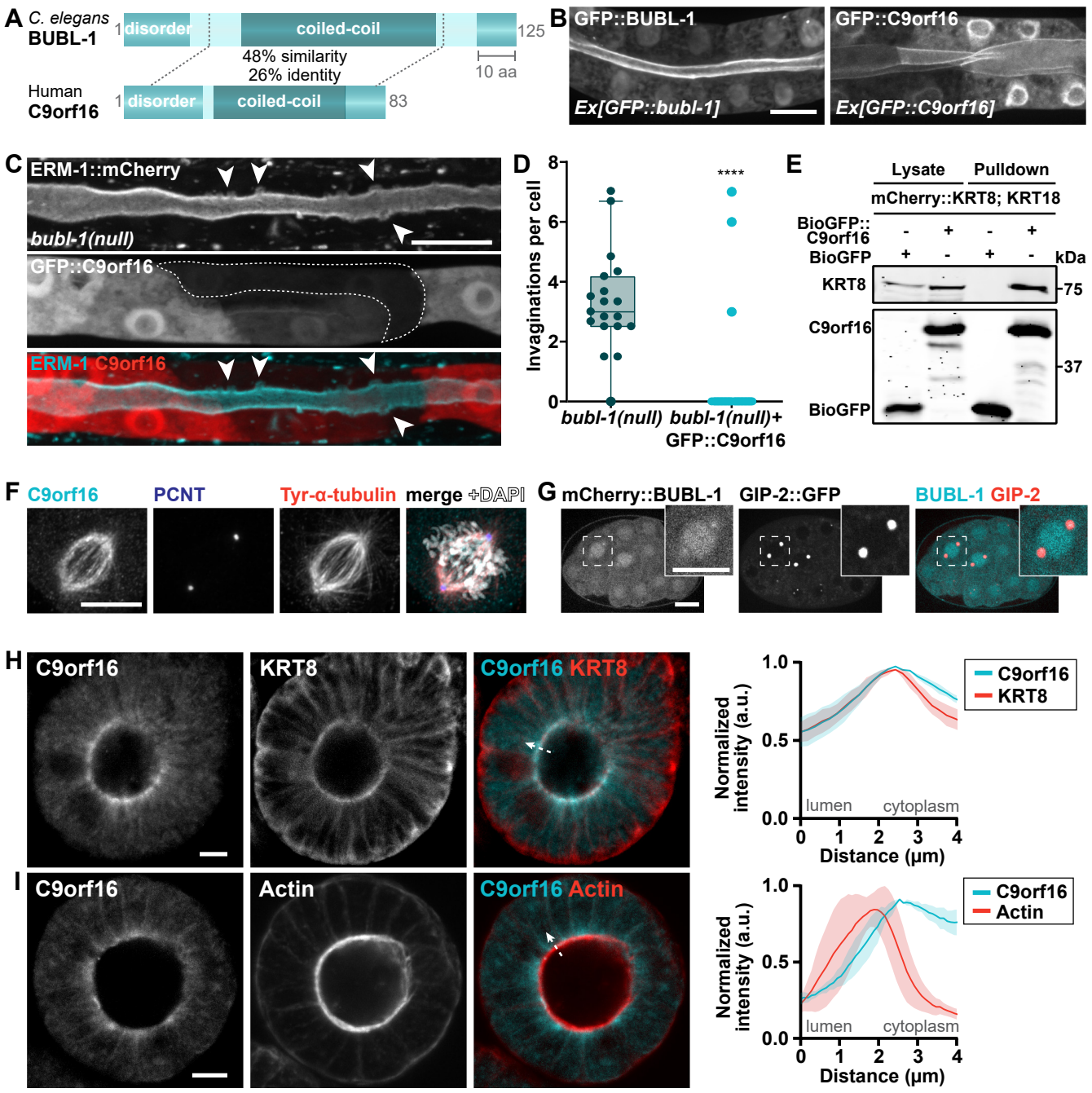

Figure 7 – C9orf16 is the mammalian homologue of BUBL-1. (**A**) Schematic representation of *C. elegans* BUBL-1 and human C9orf16 proteins with predicted domains. EMBOSS Water analysis calculates 26% identity and 48% similarity over a length of 77 aa. (**B**) Overexpression of GFP::BUBL-1 and GFP::C9orf16 in *C. elegans* under control of the intestine-specific *vha-6* promoter. (**C**) Apical membrane morphology visualized by ERM-1::mCherry in a *bubl-1(null)* L1 larva with mosaic expression of GFP::C9orf16 from an extrachromosomal array. The cell without GFP::C9orf16 expression (dotted outline) displays cytoplasmic invaginations (arrowheads). (**D**) Quantification of the number of invaginations in intestinal cells in *bubl-1(null)* L1 larvae that either express or do not express intestinal GFP::C9orf16. Each dot corresponds to a single cell (19 cells over 8 animals for control, 38 cells over 16 animals for the rescue). Data is presented as median ± interquartile range with Tukey whiskers, and data is analyzed with Mann-Whitney test; **** = P < 0.0001. (**E**) Western blots of Biotin pull-down from extracts of HEK293T cells transfected with BirA, mCherry::KRT8, KRT18 and either BioGFP::C9orf16 or BioGFP alone as control. Blots were probed for KRT8 (top) and GFP (bottom). The input is 20% of the biotin pull-down. (**F**) Point-scanning confocal microscopy images of HeLa cell stained with antibodies for C9orf16, pericentrin (PCNT) and tyrosinated α-tubulin. (**G**) Endogenous mCherry::BUBL-1 and GIP-2::GFP distribution during cell division in the early *C. elegans* embryo. (**H, I**) Section of mouse small intestinal organoid stained with antibodies against C9orf16 and Keratin 8 (KRT8, top) or with phalloidin to visualize actin (bottom). Images were acquired using point-scanning confocal microscopy. Graphs to the right show the fluorescence intensity from lumen to cytoplasm (example indicated with the dotted arrow). Fluorescent intensity was measured across all cells that are in focus, and displayed as mean ± SD.

BUBL-1 interaction screen (Fig. S4B, 4D). We additionally found subunit F of this complex (ATP6V1F), the ortholog of the high-confidence BUBL-1 interactor VHA-9. Thus, the similarity in interactions between BUBL-1 and C9orf16 extends to V-ATPase subunits, further strengthening that C9orf16 is the ortholog of BUBL-1.

Finally, we investigated the subcellular localization of C9orf16 in mammalian cells using a GFP::C9orf16 expression construct and a polyclonal antibody directed against human C9orf16. We first confirmed specificity of the antibody by immunostaining HeLa cells transfected with a GFP::C9orf16 expression construct. The staining and GFP fluorescence patterns overlapped, demonstrating that the antibody recognizes C9orf16 (Fig. S4C). We next stained HeLa cells with antibodies recognizing C9orf16 and KRT8. However, we did not detect overlap between the C9orf16 and Keratin 8 localization patterns (Fig. S4D). Thus, whereas *C. elegans* BUBL-1 appears to exclusively co-localize with intermediate filaments, this is not the case for C9orf16. Interestingly, in dividing HeLa cells, C9orf16 localized to interpolar and kinetochore microtubules, a localization we had not observed for BUBL-1 (Fig. 7F). We therefore re-examined the localization of BUBL-1 in *C. elegans* embryonic mitotic cells also expressing the γ-tubulin interacting protein GIP-2::GFP to mark the centrosomes. BUBL-1 was enriched at the interpolar region (Fig. 7G), indicating that both BUBL-1 and C9orf16 operate at the mitotic spindle.

HeLa cells do not contain the subapical IF web present in *C. elegans* intestinal cells or in differentiated enterocytes. We reasoned that the lack of co-localization between C9orf16 and Keratin 8 might reflect the absence of this particular IF structure. We therefore examined the localization of C9orf16 in mouse small intestinal organoids, which mimic the normal structure and composition of the intestinal epithelium much more closely than traditional cell cultures. In organoids, C9orf16 showed clear enrichment at the apical domain of intestinal epithelial cells. C9orf16 localized just below the apical actin network, at the same level as Keratin 8 (Fig. 7H, I). Thus, the localization of C9orf16 in mouse intestinal organoids mimics that of BUBL-1 in *C. elegans* intestinal cells. Collectively, the overlap in localization, rescue of phenotype, and similarity in interaction partners, strongly suggest that C9orf16 is the mammalian ortholog of *C. elegans* BUBL-1.

Discussion

Formation and maintenance of tubular architecture is a complex and dynamic morphogenetic process that relies on apically localized structural components conserved across animal species. Using an unbiased approach in the animal model *C. elegans* we identified the small protein BUBL-1 as a regulator of tubular architecture of the intestinal epithelium. Loss of BUBL-1 causes bubble-shaped invaginations of the apical plasma membrane into the cytoplasm, characterized by aggregation of IFs into a network of fibers that outline these protrusions. Ultrastructurally, loss of BUBL-1 results in endotube thickening between invaginations and endotube loss at invaginating membrane regions. In contrast to the severe defects in IF organization, actin, cell polarity markers, and cell junctions are largely unaffected. Similar observations were made in a dissertation that describes the identification of a mutant carrying the same point mutation present in *bubl-1(mib42)* (Paulson, 2009).

We identified C9orf16 as the mammalian ortholog of BUBL-1 based on sequence homology. When expressed in the intestine of *C. elegans*, the localization pattern of C9orf16 mimicked that of BUBL-1, including the IF-dependent apical localization. Moreover, expression of C9orf16 was able to partially suppress the *bubl-1* phenotype, delaying the appearance of invaginations. Affinity purification and mass spectrometry experiments also showed a strong overlap in candidate interaction partners between BUBL-1 and C9orf16. Finally, in mouse intestinal organoids we observed localization of C9orf16 to the apical IF network, just below the actin-rich terminal web. All of these observations are consistent with C9orf16 being the ortholog of BUBL-1. Nevertheless, while BUBL-1 seems to strictly co-localize with IFs in *C. elegans*, this is not the case for C9orf16, as we did not observe co-localization with KRT8 in HeLa cells. Thus, while C9orf16 may regulate

IF organization, its functioning may have diverged between *C. elegans* and mammals.

Multiple observations support that BUBL-1 is a direct regulator of IFs, and that the cytoplasmic invaginations in *bubl-1* mutants are a consequence of a disorganized IF network organization. First, BUBL-1 colocalizes with IFs, in a manner dependent on the presence of an IF network. Multiple IF proteins co-purified with BUBL-1 from *C. elegans* lysates, indicating that the localization of BUBL-1 is mediated through physical interactions. Second, phenotypes similar to *bubl-1(null)* have been described for mutants of the IF member *ifd-2,* and for *sma-5*, a regulator of the IF network whose loss causes cytoplasmic invaginations that are strikingly similar to those present in *bubl-1* mutants (Carberry et al., 2012; Geisler et al., 2016, 2020). Finally, and most strikingly, loss of the apical IF network through knockout of *ifb-2* suppressed the *bubl-1* phenotype, demonstrating that the presence of apical IFs is a prerequisite for invagination formation. The most likely explanation is that *bubl-1* causes an altered, pathogenic IF network state that leads to the formation of invaginations into the cytoplasm.

Why a compromised IF network leads to cytoplasmic invaginations is not clear. One explanation is that pressure from the lumen physically forces invaginations through weak spots in the IF network. However, *ifb-2* mutants which lack an apical IF network entirely, have a largely normal intestinal morphology and do not show lumen widening until the L4 stage (Geisler et al., 2020). Possibly the actin network compensates for the loss of the IF network and delimits luminal widening. The presence of compensatory mechanisms involving actin is supported by the observation that loss of *ifb-2* leads to an increase in apical levels of the actin-bundling protein PLST-1/Plastin 1 (Geisler et al., 2020). Another explanation for the formation of invaginations is that the IF network plays a more direct instructive role in determining the width of the lumen or the surface area of the apical membrane. Such a role has recently been proposed for the excretory canal, where IFs work in conjunction with actin and tubulin to control intracellular lumenogenesis (Khan et al., 2019). Here, IFs are hypothesized to regulate access of membrane formation promoting vesicles to the lumen, to restrain lateral lumen expansion. Defects in apical membrane trafficking in the intestine have been shown to cause ectopic lateral lumen formation (Shafaq-Zadah et al., 2012). Hence, it is possible that the IF network plays a role in apical trafficking in the intestine.

The molecular nature of the change to the IF network in *bubl-1* and the phenotypically very similar *sma-5* mutants also remains to be determined. SMA-5 is a stress-activated MAPK homolog, and its loss results in increased phosphorylation of IFs. Hence it likely exerts an indirect effect on IFs, but relevant downstream targets have not been identified. We therefore considered the possibility that BUBL-1 acts downstream of SMA-5. However, the increased phenotype severity we observed when *sma-5* was depleted in the *bubl-1(null)* background suggests that these genes do not act in a simple linear pathway. The protein sequence of BUBL-1 does not clearly hint at its function, as it lacks functionally distinct domains. Possible roles for BUBL-1 include cross-linking or stabilizing IF filaments, and anchoring of IFs to components of the overlying terminal web. The tendency of invaginations to occur at cell junctions may also indicate a role in linking IFs to cell junctions. However, our FRAP data indicates that BUBL-1 associates dynamically with the IF layer. Hence, the activities of BUBL-1 may be more indirect, for example localizing unidentified regulators to the IF network or promoting post-translational modifications of IF proteins. Our interaction studies identified subunits of V-ATPases as prominent candidate interactors of BUBL-1 and C9orf16. Whether these interactions are physiologically relevant and if they are involved in IF regulation or other aspects of BUBL-1 function remains to be determined. A final intriguing hypothesis is that BUBL-1 is involved in protein aggregation. C9orf16 was found in a search for highly heat-resistant proteins that remain soluble upon boiling (Tsuboyama et al., 2020). The identified proteins, termed 'Hero' for heat-resistant obscure proteins, were shown to protect different subsets of proteins from aggregation or denaturation under stress conditions (Tsuboyama et al., 2020). Indeed, C9orf16 is differentially expressed in diseases characterized by protein aggregation, including amyotrophic lateral sclerosis (ALS) (Nijssen et al., 2018), Alzheimer's (Kong et al., 2009),

and Parkinson's disease (Kim et al., 2020). As the loss of BUBL-1 leads to IF aggregation, a potential future avenue of investigation is to examine if BUBL-1 plays a direct role in protecting against protein aggregation.

In summary, we identified a conserved regulator of IF organization, whose functioning highlights the importance of IF network integrity in maintaining regular lumen shape. While our study has focused on the role of BUBL-1 in organization of the apical IF network of intestinal cells, it is likely that BUBL-1 plays additional roles in different tissues and processes. The BUBL-1 localization pattern in other tissues strongly resembled that of IFs, and the sub-apical localization of BUBL-1 in the excretory canals depended on IFC-2. Thus, BUBL-1 may be a broad regulator of IF organization in *C. elegans*.

Acknowledgments

We thank R. Schmidt for sharing strain BOX459, V. Garcia Castiglioni for strains BOX251 and BOX260, K. Oegema for strain OD2509, J. Sepers for the NRFL-1::mCherry fusion, and B. van der Vaart for the keratin plasmids. We thank M. Kersten, J.-P. ten Klooster, W. Nijenhuis, and N. Schwarz for technical assistance. We thank S. van den Heuvel, S. Ruijtenberg, M. Harterink, B. Mulder, B. Snel and members of the Van den Heuvel and Boxem groups for helpful discussions. We also thank the Biology Imaging Center, Faculty of Sciences, Department of Biology, Utrecht University. Some strains were provided by the Caenorhabditis Genetics Center, which is funded by NIH Office of Research Infrastructure Programs (P40 OD010440).

Funding

This work was supported by the Netherlands Organization for Scientific Research (NWO)-CW ECHO 711.014.005 and NWO-VICI 016.VICI.170.165 grants to M. Boxem, and the German Research Council (LE566/14-1, 3; R. Leube). This research was part of the Netherlands X-omics Initiative and partially funded by NWO, project 184.034.019.

Author Contributions

Conceptualization: S.R., J.J.R., M.B.; Formal analysis: S.R., R.S., M.B.; Investigation: S.R., F.G., R.S., J.R.K., S.v.d.H., O.D.J., M.P., J.J.R.; Resources: S.v.d.H., A.A., C.A.R., M.A., R.E.L., M.B.; Data Curation: S.R., J.R.K.; Writing – Original Draft: S.R., J.J.R., M.B.; Writing – Review & Editing: F.G., A.A., C.A.R., R.E.L.; Visualization: S.R., M.B.; Supervision: S.R., F.G., A.A., C.A.R., M.A., R.E.L., J.J.R., M.B.; Project Administration: M.B.; Funding Acquisition: A.A., C.A.R., M.A., R.E.L., M.B.

Declaration of Interests

The authors declare no competing interests.

Materials and Methods

Caenorhabditis elegans strains and culture conditions

Caenorhabditis elegans strains were cultured under standard conditions (Brenner, 1974). All experiments were performed with animals grown on nematode growth medium (NGM) agar plates at 20 °C. Ta-

ble S1 contains a list of all the strains used. Transgenic lines were generated by injecting 15 ng/µl of either plasmid pSMR10 or pSMR30 together with 65 ng/µl lambda DNA (Thermo Scientific) into the gonads of young adults.

Cell line culture

HeLa and HEK293T cell lines were cultured in DMEM/Ham's F10 (50:50) supplemented with 10% FCS and 1% penicillin/streptomycin at 37 °C and 5% CO2. All cell lines routinely tested negative for mycoplasma.

Organoid culture

Mouse small intestinal organoids derived from the duodenum of C57BL/6 mice were cultured in ENR medium: Advanced DMEM/F12 (Invitrogen) with 1% Penicillin/Streptomycin (P/S, Lonza), 1% Hepes buffer (Invitrogen) and 1% Glutamax (Invitrogen), supplemented with 5% R-spondin conditioned medium, 10% Noggin conditioned medium, 50 ng/ml EGF (Invitrogen), 1x B27 (Invitrogen), 1.25 mM n-Acetyl Cysteine (Sigma-Aldrich).

Isolation and initial mapping of mib41 and mib42

L4 stage *erm-1::GFP* animals were incubated for 6 hours at room temperature (RT) in M9 buffer (0.22 M KH_2PO_4, 0.42 M Na_2HPO_4, 0.85 M NaCl, 0.001 M $MgSO_4$) supplemented with 50 mM ethyl methanesulfonate (EMS), in a 15 ml tube with gentle rotation. Mutagenized L4 animals were placed on 9 cm NGM agar plates seeded with *E. coli* (35 plates, 10 animals per plate) and allowed to lay eggs. Parents were removed after ~1000 F1 progeny had been produced. Three days after F1 progeny started egg-laying, all F1 adults and L2 larvae were washed off the plate, leaving behind a semi-synchronous population of F2 embryos. F2 animals were allowed to develop for 2–4 days at 20 °C and scored for intestinal morphology defects using a Leica MZ16 fluorescence stereoscope. Two mutants, *mib41* and *mib42*, were isolated and backcrossed with N2 males 3 times before further analysis. To identify an approximate genetic location for both mutations, single-nucleotide polymorphism (SNP) mapping using the polymorphic strain CB4856 was performed as described previously (Davis et al., 2005).

Genomic DNA purification

C. elegans lysis and genomic DNA purification were performed using the DNeasy Blood and Tissue kit (Qiagen). Animals from two recently starved populations were collected, pooled, washed twice using M9, and resuspended in 400 µl of lysis (ATL) buffer. Samples were then flash-frozen in liquid nitrogen and stored overnight at -80 °C. After three rounds of liquid nitrogen freeze-thawing, proteinase K was added to a final concentration of 2 mg/ml and samples were incubated for 3 hours at 56 °C while shaking at 600 rpm. Samples were further incubated with 2 mg/ml RNAse A for 30 min at RT and for 10 min at 56 °C after addition of 400 µl of AL buffer. Finally, samples were mixed with 400 µl of 100% ethanol and loaded into purification columns. Wash and elution steps were performed according to the manufacturer's instructions. Concentration of genomic DNA samples was measured using Qubit Fluorometric Quantification (Invitrogen).

Identification of mib41 and mib42 mutations

We used the sibling subtraction method to identify the causative *mib41* and *mib42* mutations by whole-genome sequencing (WGS) (Joseph et al., 2018). From heterozygous *erm-1::GFP/+; mib41/+* or *erm-1::GFP/+;*

mib42/+ hermaphrodites we isolated homozygous *mib41* or *mib42* mutant, homozygous nonmutant, or heterozygous F2 progeny. Genomic DNA was then purified from pooled F3 progeny derived from 12–16 F2 animals and sequenced on an Illumina HiSeq X Ten platform. Candidate causative variants were defined as present at a frequency >0.8 in the homozygous mutant sample, <0.8 in the heterozygous sample, and <0.1 in the homozygous wild-type sample. For both mutant alleles, only a single variant from the resulting selection was predicted to affect a protein coding sequence, which was selected for further analysis. See Supplemental methods for a complete description of the bioinformatics pipeline to identify variants.

Protein structure and domain predictions

General protein domain searches were done using the SMART service at http://smart.embl-heidelberg.de/. Coiled-coils predictions were done using DeepCoil at https://toolkit.tuebingen.mpg.de/#/tools/deepcoil. Disorder predictions were done using DisEMBL at http://dis.embl.de/. Default settings were used.

Phylogenetic analysis

To identify proteins related to C15C7.5/BUBL-1, we performed a three-iteration HMMER search against the Reference Proteomes dataset at http://www.ebi.ac.uk/Tools/hmmer/.

Molecular cloning

SapTrap assembly was done as described (Schwartz and Jorgensen, 2016) using existing SEC donor modules (Dickinson et al., 2018) or new donor modules generated by cloning PCR fragments or custom gBlocks (IDT) into Eco53kI-digested vector pHSG298 (Takara Biosciences). For the *Pvha-6::GFP::bubl-1::tbb-2 3'UTR* and *Pvha-6::GFP::C9orf16::tbb-2 3'UTR* rescue constructs, *Pvha-6* was amplified from genomic N2 DNA, *GFP* and the *tbb-2 3'UTR* were amplified from prior plasmids, and the *bubl-1* and *C9orf16* sequences were synthesized as gBlocks (IDT). GFP sequence is codon-optimized and contains 3 artificial introns. A list of all used oligonucleotides (IDT) and gBlocks (IDT) is included in Table S2 and used plasmids are listed in Table S3. PCR fragments were generated using Q5 Hot Start High-Fidelity DNA Polymerase (New England Biolabs) and gel purified using the Nucleospin kit (Machery-Nagel). DNA concentrations were measured using a BioPhotometer D30 (Eppendorf). All DNA vectors used for genome editing were purified from DH5α *E. coli* using a Qiagen midiprep kit. Annotated DNA files of all plasmids used are included in Supplemental DNA files.

CRISPR/Cas9 genome engineering

Endogenous gene fusions were generated in an N2 background by homology-directed repair of CRISPR/Cas9-induced DNA double-strand breaks (DSBs). Microinjection of young adult hermaphrodite germlines was done using an inverted microinjection setup (Eppendorf FemtoJet 4x mounted on a Zeiss Axio Observer A.1 equipped with an Eppendorf Transferman 4r). In cases where the sgRNA target site was not disrupted by sequence integration, silent mutations were incorporated to prevent repeated DNA cleavage. In all cases correct integration was confirmed by Sanger sequencing (Macrogen). A list of all DNA- and RNA-based reagents is included as Table S2.

erm-1::mCherry was generated using the SEC method, using a plasmid-based repair template. sgRNA expression plasmids were generated by ligating annealed oligo pairs into BbsI-digested pJJR50 as previously described (Waaijers et al., 2016). The repair template was assembled into pMLS257 (Addgene #73716) using SapTrap with custom and SEC modules as follows (from 5' to 3'): left homology arm, a C-terminal linker (pMLS287), mCherry, SEC (pDD363), auxin-inducible degron (AID; pDD398), and right homology arm.

Homology arms of ~600 bp upstream and downstream of the DSB were amplified from N2 genomic DNA. The injection mix contained: 60 ng/µl *Peft-3::Cas9* (Addgene #46168), 15 ng/µl repair template, 100 ng/µl for each sgRNA, and 2.5 ng/µl *Pmyo-2::mCherry* (Addgene #19327). Three injected animals were pooled and incubated for 3 days at 20 °C before adding 250 ng/µl of hygromycin per plate. Rol animals lacking visible mCherry expression were selected after 4–5 days. To eliminate the selection cassette through Cre-Lox recombination, L1 progeny of selected homozygous Rol animals were heat-shocked in a water bath at 34 °C for 1 hour. Correct excision was confirmed by selection of non-Rol animals and subsequent Sanger sequencing. Sequence files of the final gene fusions are included in Supplemental DNA Files.

The *bubl-1(mib70)*, *GFP::bubl-1,* and *ifb-2::mCherry* alleles were generated using the plasmid-free nested-CRISPR approach (Vicencio et al., 2019). Injection mixes contained the following reagents (IDT): 250 ng/µl Alt-R S.p. Cas9 Nuclease V3 (IDT), 2 µM step 1 ssODN repair template, 400 ng/µl step 2 PCR repair template, 4.5-5 µM step 1 and step 2 crRNAs, 10 µM tracrRNA, as well as 1 µM *dpy-10* crRNA and ssODN repair for co-CRISPR selection (Arribere et al., 2014). Reagents for *dpy-10* co-CRISPR selection were omitted in *ifb-2::mCherry* injection mixes, and for *bubl-1(mib70)* only step 1 editing events were selected. To select for integration events, injected animals were transferred to individual plates and allowed to recover at 20 °C overnight before incubation at 25 °C for 2–3 days. F1 animals were either visually screened for presence of fluorescence using a Leica MZ16 fluorescence stereomicroscope, or singled from plates with high numbers of Dpy and Rol animals followed by PCR screening.

All other strains were produced using a plasmid-free protocol incorporating melting of double stranded DNA (dsDNA) repair templates (Ghanta and Mello, 2020). Selection of positive editing events was done by visually screening for expression of fluorescent protein, or by PCR analysis of single animals from plates with high numbers of Rol animals.

Light microscopy

Imaging of *C. elegans* was done by mounting embryos or larvae on a 5% agarose pad in a 10 mM Tetramisole solution in M9 buffer to induce paralysis. Spinning disk confocal imaging was performed using a Nikon Ti-U microscope equipped with a Yokogawa CSU-X1-M1 confocal head and an Andor iXon DU-885 camera, using a 60x 1.4 NA objective. Time-lapse imaging for FRAP experiments was performed on a Nikon Eclipse-Ti microscope equipped with a Yokogawa CSU-X1-A1 spinning disk and a Photometrics Evolve 512 EMCCD camera, using a 100x 1.4 NA objective. Targeted photobleaching was done using an ILas system (Roper Scientific France/ PICT-IBiSA, Institut Curie). Point-scanning confocal microscopy was done on a Zeiss AiryScan LSM 880 setup using a Plan-Apochromat 63x 1.2 NA objective. C9orf16 antibody test was imaged on an upright fluorescence Nikon Eclipse Ni-U microscope using a Plan Apo Lambda 100x N.A. 1.45 oil objective. Confocal imaging for KRT8 and C9orf16 in HeLa cells was performed with Leica TCS SP8 STED 3X microscope using HC PL APO 100x/1.4 oil STED WHITE objective driven by LAS X controlling software. Microscopy data was acquired using MetaMorph Microscopy Automation & Image Analysis Software (Spinning Disk), and Zen Black software (AiryScan). All stacks along the z-axis were obtained at 0.25 µm intervals. For quantifications, the same laser power and exposure times were used within experiments.

Image analysis

Invagination numbers in *bubl-1(null)* animals were counted manually from intestinal rings int2 to int4, using Z-stacks that span the entire intestinal lumen. Invagination widths were measured by determining the full width at half-maximum of an intensity plot drawn across the center of the invagination in an orthogonal view. Corresponding cell lengths were quantified by drawing a spline through the lumen from lateral membrane to lateral membrane. Intensity distribution profiles of fluorescent proteins at the apical domains of

the intestine or organoids were obtained by performing a 40-pixel (4.7 µm) wide line-scan perpendicular to the apical membrane. GFP::BUBL-1 intensity at the apical domain was determined by taking the maximum intensity value of a 40-pixel wide line-scan perpendicular to the apical membrane, and subtracting the mean background intensity (measured in a 40-pixel diameter circle outside of the worm). Each data point shown represents the average of 6–8 measurements per animal. All images were analyzed and processed using ImageJ alone (spinning disk) or in combination with Zen Black software (Airyscan).

Quantification of brood size and lethality

Starting at the L4 stage, individual P0 animals were cultured at 20 °C and transferred to a fresh plate every 24 hours for 6 days. Hatched and unhatched progeny were scored 24 hours after removal of the P0, and larval lethality was scored 48 hours after removal of the P0.

Texas Red-dextran assay

Mixed-stage populations were collected in egg buffer (118 mM NaCl, 48 mM KCl, 2 mM $MgCl_2$, 2 mM $CaCl_2$, 25 mM HEPES pH 7.3) and washed three times. The worm pellet was concentrated and resuspended in a solution containing 1 mg/ml Texas Red-dextran (40,000 MW, D1829, Molecular Probes). The samples were incubated for 90 min while shaking at 300 rpm in the dark. The dye in solution was removed by washing the samples with egg buffer until the solution was clear, and animals were either imaged directly or transferred to standard culture plates for 1 hour prior to imaging. Animals were paralyzed in 10 mM Tetramisole, transferred to a 5 % agarose pad on a glass slide, and imaged by spinning disk confocal microscopy.

FRAP experiments and analysis

For FRAP assays, laser power was adjusted in each experiment to avoid complete photobleaching of the selected area. Photobleaching was performed on a circular region with a diameter of 30 or 40 px (respectively 3.33 or 4.44 µm) at the cortex, and recovery was followed at 5 second intervals for 15 minutes. Time-lapse movies were analyzed in ImageJ. The size of the area for FRAP analysis was defined by the full width at half-maximum of an intensity plot across the bleached region in the first post-bleach frame. For each time-lapse frame, the mean intensity value within the bleached region was determined, and the background, defined as the mean intensity of a non-bleached region outside the animal, was subtracted. The mean intensities within the bleached region were corrected for acquisition photobleaching per frame using the background-subtracted mean intensity of a similar non-bleached region at the cortex, which was normalized to the corresponding pre-bleach mean intensity. FRAP recovery was calculated as the change in corrected intensity values within the bleached region. The first frame after bleach was defined as 0, and the mean intensity of the 10 frames before bleach as 1.

Curve fitting was done using GraphPad Prism 8, on averaged recovery data per sample using non-linear regression analysis (least squares regression). One and two-phase association were tested and, in all cases, data were best fitted with a two-phase curve.

Feeding RNAi

RNAi clones for *bubl-1*, *ifb-2*, *ifc-2*, *ifd-2* and *let-413* were obtained from the genome wide Vidal full-length HT115 RNAi feeding library derived from the ORFeome 3.1 collection (Rual et al., 2004). The RNAi clone for *ifc-1* was obtained from the genome wide Ahringer fragment HT115 RNAi feeding library (Kamath et al.,

2003), supplied through Source BioScience. All clones were verified using Sanger sequencing. RNAi clones for *ifo-1*, *ifd-1*, *ifp-1* and *sma-5* were generated by subcloning the corresponding cDNA into a modified L4440 RNAi feeding vector, containing a linker with AscI and NotI restriction sites. To specifically target *act-5*, and no other actin isoforms that share extensive sequence homology, we followed a previously described strategy and designed an RNAi clone against the unique 3'UTR (MacQueen et al., 2005). For all custom RNAi clones, fragments were amplified from a cDNA library, digested with AscI/NotI, ligated into AscI/NotI-digested L4440, and transformed into *E. coli* DH5α. Single colonies were isolated, plasmid DNA was purified, and presence of an insert was confirmed by Sanger sequencing. Correct clones were re-transformed into *E. coli* HT115, again confirmed by sequencing and stored at -80 °C in 50% glycerol (1:1). All primer pairs are listed in Table S2.

For feeding RNAi experiments, bacterial clones were pre-cultured in 2 ml Lysogeny Broth (LB) supplemented with 100 µg/ml ampicillin and 2.5 µg/ml tetracycline at 37 °C while rotating at 200 rpm for 6–8 hours, and then transferred to new tubes with a total volume of 10 mL and cultured overnight. An HT115 bacterial clone expressing the L4440 vector lacking an insert was used as a control in feeding experiments. To induce production of dsRNA, cultures were incubated for 90 min in the presence of 1 mM Isopropyl β-D-1-thiogalactopyranoside (IPTG). Bacterial cultures were pelleted by centrifugation at 3220 g for 15 min and concentrated 5x. NGM agar plates supplemented with 100 µg/ml ampicillin and 1 mM IPTG were seeded with 250 µl of bacterial suspension, and kept at room temperature for 48 hour in the dark. L1 or L4 hermaphrodites were placed on the seeded RNAi plates and incubated at 20 °C (Timmons and Fire, 1998).

Electron microscopy

Young adult animals were transferred into a 100 µm deep membrane carrier containing 20% bovine serum albumin in M9 worm buffer (22 mM KH_2PO_4, 42 mM Na_2HPO_4, 86 mM NaCl, 1 mM $MgSO_4$) and then high-pressure frozen in a Leica EM Pact high-pressure freezer. A minimum of five samples with 10-20 animals were frozen per experiment. Quick freeze substitution with agitation using 1% OsO_4, 0.2% uranyl acetate in acetone followed by rapid epoxy resin embedding was performed as previously described (McDonald, 2014; Reipert et al., 2018). Subsequently, 50 nm thick sections of the embedded samples were prepared using a Leica UC7. These were contrasted for 10 min in 1% uranyl acetate in ethanol and Reynolds lead citrate and recorded at 100 kV on a Hitachi H-7600 transmission electron microscope (Tokyo, Japan).

Auxin Inducible Degradation

Auxin treatment was performed by transferring worms to NGM plates seeded with *E. coli* OP50 and containing 1 mM auxin. To prepare plates, auxin (Alfa Aesar A10556) was diluted into the autoclaved NGM agar medium after cooling to 60 °C prior to plate pouring. Plates were kept for a maximum of 2 weeks in the dark at 4 °C. To obtain semi-synchronized worm populations, 40 adults were placed on NGM plates seeded with *E. coli* OP50 and allowed to lay eggs. After 1 hour of egg laying, plates were carefully washed with M9 (0.22 M KH2 PO4 , 0.42 M Na2 HPO4 , 0.85 M NaCl, 0.001 M MgSO4) buffer in order to remove larvae and adults but leave the eggs behind.

Affinity-purification and mass spectrometry analysis

GFP pull-down from *C. elegans*. Animals endogenously expressing GFP-tagged BUBL-1 or control animals expressing an integrated GFP transgene (Waaijers et al., 2016) were grown on 6–8 9 cm NGM plates until starvation, to enrich for L1 animals. Animals were then transferred into 250 ml of S-Medium supplemented with 1% Penn/Strep (Life Technologies), 0.1% nystatin (Sigma) and OP50 bacteria obtained from the growth

of a 400 ml culture. Animals were grown at 20 °C at low shaking for 96 hours and were harvested and cleaned using a sucrose gradient, as previously described (Waaijers et al., 2016) with one exception being the inclusion of $MgSO_4$ in the M9 medium. Worms were distributed into 15 ml TPX tubes (Diagenode) to reach 200–400 µl worm pellet per tube, and were washed with lysis buffer (25mM Tris-HCl pH 7.5, 150mM NaCl, 1mM EDTA, 0.5% IGEPAL CA-630, 1X cOmplete Protease Inhibitor Cocktail (Roche)). The liquid was removed, and the sample was flash frozen in liquid nitrogen for storage at -80 °C.

To lyse the worms, tubes were thawed on ice and ice-cold lysis buffer was added to reach a total volume of 2 ml. Tubes were sonicated for 10 mins (sonication cycle: 30 sec ON, 30 sec OFF) at 4 °C in a Bioruptor ultra-sonication bath (Diagenode) at high energy setting. After lysis, lysates were cleared by centrifugation and protein levels were measured using the Bradford BCA assay (Thermo Scientific).

Immunoprecipitation was performed using GFP-Trap Magnetic Agarose beads (Chromotek) according to manufacturer's protocol, using 25 µl of beads per sample. To prep the beads, they were first equilibrated in wash buffer (10 mM Tris/Cl pH 7.5, 150 mM NaCl, 0.5 mM EDTA, 0.1% IGEPAL CA-630), blocked with 1% BSA for 1 hour, then washed 4 times with wash buffer. Next, lysate was added to the beads and they were incubated for 1 hour tumbling end-over-end. Lysate was then removed, and the beads were washed 4 times in wash buffer. After the final wash step, all liquid was removed, and the beads were flash frozen with liquid nitrogen. The experiment was performed in triplicate (biological replicates) and processed on independent days.

Biotin-streptavidin pull-down from cells. Confluent HEK293T cells were split in a 1:3 dilution 24 hours before transfection. Cells were transfected with overexpression constructs indicated in figure legend together with BirA. 1 µg/µL PEI (Polyethylenimine HCl MAX Linear MW 40000 (PolySciences, 24765–2)) and 1 µg/µL DNA (3:1) were mixed in Ham's F10 and incubated for 5 minutes at room temperature. The mixture was added to cells and incubated for 24 hours to allow expression. The cells were harvested in ice-cold PBS and lysed with lysis buffer (150 mM Tris-HCl pH 7.5, 150 mM NaCl, 1% Triton X-100 and cOmplete protease inhibitor cocktail (Roche)). 90% of each cell lysate was centrifuged at 13,000 rpm for 5 minutes and the supernatants were transferred and incubated with streptavidin beads (Dynabeads M-280, Invitrogen), which were already blocked by 0.2% Chicken Egg Albumine (Sigma). The remaining cell lysates were denatured with SDS/DTT sample buffer and used as input sample. Beads were incubated for 40 minutes at 4 °C, before washing 5 times with washing buffer (100mM Tris pH7.5, 150 mM NaCl, 0.5% Triton X-100 and 0.5x protease inhibitor cocktail).

Western blot analysis for C9orf16/Keratin pull-down. For western blot assays, pull-down samples were eluted with SDS/DTT sample buffer and boiled for 5 min at 95 °C. Both pull-down and input were loaded into 10% SDS-PAGE gels and transferred to nitrocellulose membrane. Membranes were blocked with 2% BSA (bovine serum albumin) in PBS/0.05% Tween-20. Primary antibodies were diluted in blocking buffer and incubated with the membranes overnight at 4 °C, washed 3 times with PBS/0.05% Tween-20 and incubated with IRDye 680LT and IRDye 800CW antibodies (LI-COR Biosciences) for 45 min at RT. Membranes were washed 3 times with PBS/0.05% Tween-20 before imaging on an Odyssey Infrared Imaging system (LI-COR Biosciences).

Mass spectrometry analysis for BUBL-1/C9orf16. Streptavidin and anti-GFP beads after affinity purification were resuspended in 15 µl of 4× Laemmli sample buffer (Biorad), boiled at 99 °C for 10 min and supernatants were loaded on 4–12% Criterion XT Bis–Tris precast gel (Biorad). The gel was fixed with 40% methanol and 10% acetic acid and then stained for 1 hour using colloidal coomassie dye G-250 (Gel Code Blue Stain, Thermo Scientific). Each lane from the gel was cut and placed in 1.5 ml tubes. Samples were then washed with 250 µl of water, followed by 15 min dehydration in acetonitrile. Proteins were reduced (10mM DTT, 1

hour at 56 °C), dehydrated and alkylated (55mM iodoacetamide, 1 hour in the dark). After two rounds of dehydration, trypsin was added to the samples and incubated overnight at 37 °C. Peptides were extracted with acetonitrile, dried down and reconstituted in 10% formic acid prior to MS analysis.

Samples were analyzed on an Orbitrap Q-Exactive mass spectrometer (Thermo Fisher Scientific) coupled to an Agilent 1290 Infinity LC (Agilent Technologies). Peptides were loaded onto a trap column (Reprosil pur C18, Dr. Maisch, 100 µm × 2 cm, 3 µm; constructed in-house) with solvent A (0.1% formic acid in water) at a maximum pressure of 800 bar and chromatographically separated over the analytical column (Poroshell 120 EC C18, Agilent Technologies, 100 µm x 50 cm, 2.7 µm) using 90 min linear gradient from 7% to 30% solvent B (0.1% formic acid in acetonitrile) at a flow rate of 150 nl min^{-1}. The mass spectrometers were used in a data-dependent mode, which automatically switched between MS and MS/MS. After a survey scan from 375 to 1600m/z the 10 most abundant peptides were subjected to HCD fragmentation. MS spectra were acquired with a resolution > 30,000, whereas MS2 with a resolution > 17,500.

Raw data files were converted to mgf files using Proteome Discoverer 1.4 software (Thermo Fisher Scientific). Database search was performed using the *C. elegans* or the human database and Mascot (version 2.5.1, Matrix Science, UK) as the search engine. Carbamidomethylation of cysteines was set as a fixed modification and oxidation of methionine was set as a variable modification. Trypsin was set as cleavage specificity, allowing a maximum of two missed cleavages. Data filtering was performed using a percolator, resulting in 1% false discovery rate (FDR). Additional filters were search engine rank 1 and mascot ion score > 20.

Crapome (Mellacheruvu et al., 2013) was used to analyze BUBL-1 interacting proteins in three biological replicas and C9orf16 binding proteins in a single experiment, using proteins identified in the GFP pull downs as control. Significance analysis of interactome (SAINT) score (Choi et al., 2011) and simpler fold-change (FC) calculations FC-A and FC-B were derived from the Crapome analysis by averaging the spectral counts across the controls. FC-A averages the counts across all controls while the more stringent FC-B takes the average of the top 3 highest spectral counts for the abundance estimate.

Antibodies and Immunofluorescence Cell Staining

We used rabbit polyclonal antibodies against C9orf16 (Sigma-Aldrich Cat# HPA020725, RRID:AB_1845816), mouse monoclonal antibodies against PCNT (Abcam Cat# ab28144, RRID:AB_2160664), and rat monoclonal antibodies against tyrosinated α-tubulin (YL1/2; Thermo Fisher Scientific Cat# MA1-80017, RRID:AB_2210201) and KRT8 (DSHB Cat# TROMA-I, RRID:AB_531826). We used Alexa Fluor 568-conjugated Phalloidin to stain actin (Life Technologies). We used Alexa Fluor 488-, 594- and 647-conjugated goat antibodies against respectively mouse, rabbit and rat (Life Technologies) as secondary antibodies.

HeLa cells were fixed with −20 °C methanol or 4% PFA for 10 min and permeabilized with 0.1% Triton X-100 in phosphate-buffered saline (PBS) for 10 min. Subsequent washing and labeling steps were carried out in PBS supplemented with 2% bovine serum albumin and 0.05% Tween-20. Slides were rinsed in 70 and 100% ethanol and mounted in Vectashield mounting medium supplemented with DAPI (Vector Laboratories).

Mouse small intestinal organoids were fixed in suspension using ice-cold 4% PFA (Aurion) and immunolabeled as described previously (van Ineveld et al., 2020).

Statistical analysis

All statistical analyses were performed using GraphPad Prism 8. For population comparisons, a D'Agostino

& Pearson test of normality was first performed to determine if the data was sampled from a Gaussian distribution. For data drawn from a Gaussian distribution, comparisons between two populations were done using an unpaired t-test, with Welch's correction if the SDs of the populations differ significantly, and comparisons between >2 populations were done using a one-way ANOVA if the SDs of the populations differ significantly. For data not drawn from a Gaussian distribution, a non-parametric test was used (Mann-Whitney for 2 populations and Kruskal-Wallis for >2 populations). ANOVA and non-parametric tests were followed up with multiple comparison tests of significance (Dunnett's, Tukey's, Dunnett's T3 or Dunn's). Tests of significance used and sample sizes are indicated in the figure legends. No statistical method was used to pre-determine sample sizes. No samples or animals were excluded from analysis. The experiments were not randomized, and the investigators were not blinded to allocation during experiments and outcome assessment.

References

Al-Hashimi, H., Hall, D.H., Ackley, B.D., Lundquist, E.A., and Buechner, M. (2018). Tubular Excretory Canal Structure Depends on Intermediate Filaments EXC-2 and IFA-4 in *Caenorhabditis elegans*. Genetics genetics.301078.2018.

Arribere, J.A., Bell, R.T., Fu, B.X.H., Artiles, K.L., Hartman, P.S., and Fire, A.Z. (2014). Efficient Marker-Free Recovery of Custom Genetic Modifications with CRISPR/Cas9 in *Caenorhabditis elegans*. Genetics *198*, 837–846.

Asghar, M.N., Silvander, J.S.G., Helenius, T.O., Lähdeniemi, I.A.K., Alam, C., Fortelius, L.E., Holmsten, R.O., and Toivola, D.M. (2015). The Amount of Keratins Matters for Stress Protection of the Colonic Epithelium. PLOS ONE *10*, e0127436.

Bergmann, C., Guay-Woodford, L.M., Harris, P.C., Horie, S., Peters, D.J.M., and Torres, V.E. (2018). Polycystic kidney disease. Nat. Rev. Dis. Primer *4*, 50.

Bidaud-Meynard, A., Nicolle, O., Heck, M., Le Cunff, Y., and Michaux, G. (2019). A V0-ATPase-dependent apical trafficking pathway maintains the polarity of the intestinal absorptive membrane. Dev. Camb. Engl. *146*.

Bossinger, O., Fukushige, T., Claeys, M., Borgonie, G., and McGhee, J.D. (2004). The apical disposition of the Caenorhabditis elegans intestinal terminal web is maintained by LET-413. Dev. Biol. *268*, 448–456.

Brenner, S. (1974). The genetics of Caenorhabditis elegans. Genetics *77*, 71–94.

Carberry, K., Wiesenfahrt, T., Geisler, F., Stocker, S., Gerhardus, H., Uberbach, D., Davis, W., Jorgensen, E., Leube, R.E., and Bossinger, O. (2012). The novel intestinal filament organizer IFO-1 contributes to epithelial integrity in concert with ERM-1 and DLG-1. Development *139*, 1851–1862.

Choi, H., Larsen, B., Lin, Z.-Y., Breitkreutz, A., Mellacheruvu, D., Fermin, D., Qin, Z.S., Tyers, M., Gingras, A.-C., and Nesvizhskii, A.I. (2011). SAINT: probabilistic scoring of affinity purification–mass spectrometry data. Nat. Methods *8*, 70–73.

Coch, R., and Leube, R. (2016). Intermediate Filaments and Polarization in the Intestinal Epithelium. Cells *5*, 32.

Coulombe, P.A., and Wong, P. (2004). Cytoplasmic intermediate filaments revealed as dynamic and multipurpose scaffolds. Nat. Cell Biol. *6*, 699–706.

Cutting, G.R. (2015). Cystic fibrosis genetics: from molecular understanding to clinical application. Nat. Rev. Genet. *16*, 45–56.

Davis, M.W., Hammarlund, M., Harrach, T., Hullett, P., Olsen, S., and Jorgensen, E.M. (2005). Rapid single nucleotide polymorphism mapping in C. elegans. BMC Genomics *6*, 118.

Dickinson, D.J., Slabodnick, M.M., Chen, A.H., and Goldstein, B. (2018). SapTrap assembly of repair templates for Cas9-triggered homologous recombination with a self-excising cassette. Micropublication Biol. 3.

Erber, A., Riemer, D., Bovenschulte, M., and Weber, K. (1998). Molecular Phylogeny of Metazoan Intermediate Filament Proteins. J. Mol. Evol. *47*, 751–762.

Estes, K.A., Szumowski, S.C., and Troemel, E.R. (2011). Non-Lytic, Actin-Based Exit of Intracellular Parasites from C. elegans Intestinal Cells. PLoS Pathog. *7*, e1002227.

Etienne-Manneville, S. (2018). Cytoplasmic Intermediate Filaments in Cell Biology. Annu. Rev. Cell Dev. Biol. *34*, 1–28.

Geisler, F., and Leube, R.E. (2016). Epithelial Intermediate Filaments: Guardians against Microbial Infection? Cells *5*, 29.

Geisler, F., Gerhardus, H., Carberry, K., Davis, W., Jorgensen, E., Richardson, C., Bossinger, O., and Leube, R.E. (2016). A novel function for the MAP kinase SMA-5 in intestinal tube stability. Mol. Biol. Cell *27*, 3855–3868.

Geisler, F., Coch, R.A., Richardson, C., Goldberg, M., Denecke, B., Bossinger, O., and Leube, R.E. (2019). The intestinal intermediate filament network responds to and protects against microbial insults and toxins. Development *146*, dev169482.

Geisler, F., Coch, R.A., Richardson, C., Goldberg, M., Bevilacqua, C., Prevedel, R., and Leube, R.E. (2020). Intestinal intermediate filament polypeptides in C. elegans : Common and isotype-specific contributions to intestinal ultrastructure and function. Sci. Rep. *10*, 1–18.

Ghanta, K.S., and Mello, C.C. (2020). Melting dsDNA donor molecules potentiates precision genome editing in C. elegans. BioRxiv 2020.08.03.235036.

Hapiak, V., Hresko, M.C., Schriefer, L.A., Saiyasisongkhram, K., Bercher, M., and Plenefisch, J. (2003). Mua-6, a gene required for tissue integrity in Caenorhabditis elegans, encodes a cytoplasmic intermediate filament. Dev. Biol. *263*, 330–342.

Hu, Y., Flockhart, I., Vinayagam, A., Bergwitz, C., Berger, B., Perrimon, N., and Mohr, S.E. (2011). An integrative approach to ortholog prediction for disease-focused and other functional studies. BMC Bioinformatics *12*, 357.

Hüsken, K., Wiesenfahrt, T., Abraham, C., Windoffer, R., Bossinger, O., and Leube, R.E. (2008). Maintenance of the intestinal tube in Caenorhabditis elegans: the role of the intermediate filament protein IFC-2. Differentiation *76*, 881-s3.

van Ineveld, R.L., Ariese, H.C.R., Wehrens, E.J., Dekkers, J.F., and Rios, A.C. (2020). Single-Cell Resolution Three-Dimensional Imaging of Intact Organoids. J. Vis. Exp. JoVE.

Iruela-Arispe, M.L., and Beitel, G.J. (2013). Tubulogenesis. Dev. Camb. Engl. *140*, 2851–2855.

Iruela-Arispe, M.L., and Davis, G.E. (2009). Cellular and Molecular Mechanisms of Vascular Lumen Formation. Dev. Cell *16*, 222–231.

Ji, Y.J., Choi, K.Y., Song, H.-O., Park, B.-J., Yu, J.-R., Kagawa, H., Song, W.K., and Ahnn, J. (2006). VHA-8, the E subunit of V-ATPase, is essential for pH homeostasis and larval development in C. elegans. FEBS Lett. *580*, 3161–3166.

Joseph, B.B., Blouin, N.A., and Fay, D.S. (2018). Use of a Sibling Subtraction Method for Identifying Causal Mutations in Caenorhabditis elegans by Whole-Genome Sequencing. G3 GenesGenomesGenetics *8*, 669–678.

Kamath, R.S., Fraser, A.G., Dong, Y., Poulin, G., Durbin, R., Gotta, M., Kanapin, A., Le Bot, N., Moreno, S., Sohrmann, M., et al. (2003). Systematic functional analysis of the Caenorhabditis elegans genome using RNAi. Nature *421*, 231–237.

Karabinos, A., Schulze, E., Klisch, T., Wang, J., and Weber, K. (2002). Expression profiles of the essential intermediate filament (IF) protein A2 and the IF protein C2 in the nematode Caenorhabditis elegans. Mech. Dev. *117*, 311–314.

Karabinos, A., Schulze, E., Schünemann, J., Parry, D.A.D., and Weber, K. (2003). In Vivo and in Vitro Evidence that the Four Essential Intermediate Filament (IF) Proteins A1, A2, A3 and B1 of the Nematode Caenorhabditis elegans Form an Obligate Heteropolymeric IF System. J. Mol. Biol. *333*, 307–319.

Karabinos, A., Schünemann, J., and Weber, K. (2004). Most genes encoding cytoplasmic intermediate filament (IF) proteins of the nematode Caenorhabditis elegans are required in late embryogenesis. Eur. J. Cell Biol. *83*, 457–468.

Khan, L.A., Jafari, G., Zhang, N., Membreno, E., Yan, S., Zhang, H., and Gobel, V. (2019). A tensile trilayered cytoskeletal endotube drives capillary-like lumenogenesis. J. Cell Biol. *218*, 2403–2424.

Kim, S.M., Cho, S.Y., Kim, M.W., Roh, S.R., Shin, H.S., Suh, Y.H., Geum, D., and Lee, M.A. (2020). Genome-Wide Analysis Identifies NURR1-Controlled Network of New Synapse Formation and Cell Cycle Arrest in Human Neural Stem Cells. Mol. Cells *43*, 551–571.

Kong, W., Mou, X., Liu, Q., Chen, Z., Vanderburg, C.R., Rogers, J.T., and Huang, X. (2009). Independent component analysis of Alzheimer's DNA microarray gene expression data. Mol. Neurodegener. *4*, 5.

Leung, B., Hermann, G.J., and Priess, J.R. (1999). Organogenesis of the Caenorhabditis elegans Intestine. Dev. Biol. *216*, 114–134.

Lubarsky, B., and Krasnow, M.A. (2003). Tube morphogenesis: making and shaping biological tubes. Cell *112*, 19–28.

Luck, K., Kim, D.-K., Lambourne, L., Spirohn, K., Begg, B.E., Bian, W., Brignall, R., Cafarelli, T., Campos-Laborie, F.J., Charloteaux, B., et al. (2020). A reference map of the human binary protein interactome. Nature *580*, 402–408.

MacQueen, A.J., Baggett, J.J., Perumov, N., Bauer, R.A., Januszewski, T., Schriefer, L., and Waddle, J.A. (2005). ACT-5 Is an Essential Caenorhabditis elegans Actin Required for Intestinal Microvilli Formation□D. Mol. Biol. Cell *16*, 13.

McDonald, K.L. (2014). Rapid embedding methods into epoxy and LR White resins for morphological and immunological analysis of cryofixed biological specimens. Microsc. Microanal. Off. J. Microsc. Soc. Am. Microbeam Anal. Soc. Microsc. Soc. Can. *20*, 152–163.

Mellacheruvu, D., Wright, Z., Couzens, A.L., Lambert, J.-P., St-Denis, N.A., Li, T., Miteva, Y.V., Hauri, S., Sardiu, M.E., Low, T.Y., et al. (2013). The CRAPome: a contaminant repository for affinity purification–mass spectrometry data. Nat. Methods *10*, 730–736.

Munn, E.A., and Greenwood, C. a. (1984). The occurrence of submicrovillar endotube (modified terminal web) and associated cytoskeletal structures in the intestinal epithelia of nematodes. Philos. Trans. R. Soc. Lond. B Biol. Sci. *306*, 1–18.

Nijssen, J., Aguila, J., Hoogstraaten, R., Kee, N., and Hedlund, E. (2018). Axon-Seq Decodes the Motor Axon Transcriptome and Its Modulation in Response to ALS. Stem Cell Rep. *11*, 1565–1578.

Nishimura, K., Fukagawa, T., Takisawa, H., Kakimoto, T., and Kanemaki, M. (2009). An auxin-based degron system for the rapid depletion of proteins in nonplant cells. Nat. Methods *6*, 917–922.

Pasti, G., and Labouesse, M. (2014). Epithelial junctions, cytoskeleton, and polarity. WormBook 1–35.

Paulson, C.C. (2009). Analysis of C. elegans genes required for maintaining intestinal lumen morphology and ingested drug resistance. Southern Methodist University.

Potter, S.C., Luciani, A., Eddy, S.R., Park, Y., Lopez, R., and Finn, R.D. (2018). HMMER web server: 2018 update. Nucleic Acids Res. *46*, W200–W204.

Ramalho, J.J., Sepers, J.J., Nicolle, O., Schmidt, R., Cravo, J., Michaux, G., and Boxem, M. (2020). C-terminal phosphorylation modulates ERM-1 localization and dynamics to control cortical actin organization and support lumen formation during C. elegans development. Dev. Camb. Engl.

Ramos, G.P., and Papadakis, K.A. (2019). Mechanisms of Disease: Inflammatory Bowel Diseases. Mayo Clin. Proc. *94*, 155–165.

Reipert, S., Goldammer, H., Richardson, C., Goldberg, M.W., Hawkins, T.J., Hollergschwandtner, E., Kaufmann, W.A., Antreich, S., and Stierhof, Y.-D. (2018). Agitation Modules: Flexible Means to Accelerate Automated Freeze Substitution. J. Histochem. Cytochem. Off. J. Histochem. Soc. *66*, 903–921.

Rolland, T., Taşan, M., Charloteaux, B., Pevzner, S.J., Zhong, Q., Sahni, N., Yi, S., Lemmens, I., Fontanillo, C., Mosca, R., et al. (2014). A Proteome-Scale Map of the Human Interactome Network. Cell *159*, 1212–1226.

Rual, J.-F., Ceron, J., Koreth, J., Hao, T., Nicot, A.-S., Hirozane-Kishikawa, T., Vandenhaute, J., Orkin, S.H., Hill, D.E., Heuvel, S. van den, et al. (2004). Toward Improving Caenorhabditis elegans Phenome Mapping With an ORFeome-Based RNAi Library. Genome Res. *14*, 2162–2168.

Rual, J.-F., Venkatesan, K., Hao, T., Hirozane-Kishikawa, T., Dricot, A., Li, N., Berriz, G.F., Gibbons, F.D., Dreze, M., Ayivi-Guedehoussou, N., et al. (2005). Towards a proteome-scale map of the human protein-protein interaction network. Nature *437*, 1173–1178.

Salas, P.J., Forteza, R., and Mashukova, A. (2016). Multiple roles for keratin intermediate filaments in the regulation of epithelial barrier function and apico-basal polarity. Tissue Barriers *4*, e1178368.

Sanghvi-Shah, R., and Weber, G.F. (2017). Intermediate Filaments at the Junction of Mechanotransduction, Migration, and Development. Front. Cell Dev. Biol. *5*.

Schelling, J.R. (2016). Tubular atrophy in the pathogenesis of chronic kidney disease progression. Pediatr. Nephrol. Berl. Ger. *31*, 693–706.

Schwartz, M.L., and Jorgensen, E.M. (2016). SapTrap, a Toolkit for High-Throughput CRISPR/Cas9 Gene Modification in *Caenorhabditis elegans*. Genetics *202*, 1277–1288.

Schwarz, N., Windoffer, R., Magin, T.M., and Leube, R.E. (2015). Dissection of keratin network formation, turnover and reorganization in living murine embryos. Sci. Rep. *5*, 9007.

Shafaq-Zadah, M., Brocard, L., Solari, F., and Michaux, G. (2012). AP-1 is required for the maintenance of apico-basal polarity in the C. elegans intestine. Development *139*, 2061–2070.

Sigurbjörnsdóttir, S., Mathew, R., and Leptin, M. (2014). Molecular mechanisms of de novo lumen formation. Nat. Rev. Mol. Cell Biol. *15*, 665–676.

Stutz, K., Kaech, A., Aebi, M., Künzler, M., and Hengartner, M.O. (2015). Disruption of the C. elegans Intestinal Brush Border by the Fungal Lectin CCL2 Phenocopies Dietary Lectin Toxicity in Mammals. PLOS ONE *10*, e0129381.

Sulston, J.E., Schierenberg, E., White, J.G., and Thomson, J.N. (1983). The embryonic cell lineage of the nematode Caenorhabditis elegans. Dev. Biol. *100*, 64–119.

Sundaram, M.V., and Buechner, M. (2016). The Caenorhabditis elegans Excretory System: A Model for Tubulogenesis, Cell Fate Specification, and Plasticity. Genetics *203*, 35–63.

Timmons, L., and Fire, A. (1998). Specific interference by ingested dsRNA. Nature *395*, 854.

Toivola, D.M., Strnad, P., Habtezion, A., and Omary, M.B. (2010). Intermediate filaments take the heat as stress proteins. Trends Cell Biol. *20*, 79–91.

Tsuboyama, K., Osaki, T., Matsuura-Suzuki, E., Kozuka-Hata, H., Okada, Y., Oyama, M., Ikeuchi, Y., Iwasaki, S., and Tomari, Y. (2020). A widespread family of heat-resistant obscure (Hero) proteins protect against protein instability and aggregation. PLOS Biol. *18*, e3000632.

Vicencio, J., Martínez-Fernández, C., Serrat, X., and Cerón, J. (2019). Efficient Generation of Endogenous Fluorescent Reporters by Nested CRISPR in Caenorhabditis elegans. Genetics *211*, 1143–1154.

Waaijers, S., Muñoz, J., Berends, C., Ramalho, J.J., Goerdayal, S.S., Low, T.Y., Zoumaro-Djayoon, A.D., Hoffmann, M., Koorman, T., Tas, R.P., et al. (2016). A tissue-specific protein purification approach in Caenorhabditis elegans identifies novel interaction partners of DLG-1/Discs large. BMC Biol. *14*, 66.

Watanabe, N., Nagamatsu, Y., Gengyo-Ando, K., Mitani, S., and Ohshima, Y. (2005). Control of body size by SMA-5, a homolog of MAP kinase BMK1/ERK5, in C. elegans. Development *132*, 3175–3184.

Weber, K., Plessmann, U., and Ulrich, W. (1989). Cytoplasmic intermediate filament proteins of invertebrates are closer to nuclear lamins than are vertebrate intermediate filament proteins; sequence characterization of two muscle proteins of a nematode. EMBO J. *8*, 3221–3227.

Williams, K., Williams, K., Baucher, H.M., and Plenefisch, J. (2015). The Tail Domain Is Essential but the Head Domain Dispensable for C. elegans Intermediate Filament IFA-2 Function. PLOS ONE *10*, e0119282.

Woo, W.-M., Goncharov, A., Jin, Y., and Chisholm, A.D. (2004). Intermediate filaments are required for C. elegans epidermal elongation. Dev. Biol. *267*, 216–229.

Zdobnov, E.M., Tegenfeldt, F., Kuznetsov, D., Waterhouse, R.M., Simão, F.A., Ioannidis, P., Seppey, M., Loetscher, A., and Kriventseva, E.V. (2017). OrthoDB v9.1: cataloging evolutionary and functional annotations for animal, fungal, plant, archaeal, bacterial and viral orthologs. Nucleic Acids Res. *45*, D744–D749.

Zhang, L., Ward, J.D., Cheng, Z., and Dernburg, A.F. (2015). The auxin-inducible degradation (AID) system enables versatile conditional protein depletion in C. elegans. Dev. Camb. Engl. *142*, 4374–4384.